

1 **TPHiPr: A long-term (1979-2020) high-accuracy precipitation dataset (1/30 °, daily) for the Third**
2 **Pole region based on high-resolution atmospheric modeling and dense observations**

3 Yaozhi Jiang¹, Kun Yang^{1,2*}, Youcun Qi³, Xu Zhou², Jie He², Hui Lu¹, Xin Li², Yingying Chen²,
4 Xiaodong Li⁴, Bingrong Zhou⁵, Ali Mamtimin⁶, Changkun Shao¹, Xiaogang Ma¹, Jiabin Tian¹,
5 Jianhong Zhou¹

6 ¹ Department of Earth System Science, Ministry of Education Key Laboratory for Earth System
7 Modeling, Institute for Global Change Studies, Tsinghua University, Beijing, China.

8 ² National Tibetan Plateau Data Center, State Key Laboratory of Tibetan Plateau Earth System,
9 Environment and Resources, Institute of Tibetan Plateau Research, Chinese Academy of Sciences,
10 Beijing, China.

11 ³ Key Laboratory of Water Cycle and Related Land Surface Processes, Institute of Geographic Sciences
12 and Natural Resources Research, Chinese Academy of Sciences, Beijing, China

13 ⁴ State Key Laboratory of Hydraulics and Mountain River Engineering, Sichuan University, Chengdu,
14 China

15 ⁵ Qinghai Institute of Meteorology Science, Xining, China

16 ⁶ Institute of Desert Meteorology/Taklimakan Desert Meteorology Field Experiment Station, China
17 Meteorological Administration, Urumq, China

18 **Correspondence to:** Kun Yang (yangk@tsinghua.edu.cn)

19

20 **Abstract:** Reliable precipitation data are highly necessary for geoscience research in the Third Pole (TP)
21 region but still lacking, due to the complex terrain and high spatial variability of precipitation here.
22 Accordingly, this study produces a long-term (1979-2020) high-resolution ($1/30^\circ$, daily) precipitation
23 dataset (TPHiPr) for the TP by merging the atmospheric simulation-based ERA5_CNN with gauge
24 observations from more than 9000 rain gauges, using the Climatology Aided Interpolation and Random
25 Forest methods. Validation shows that the TPHiPr is generally unbiased and has a root mean square error
26 of 5.0 mm day^{-1} , a correlation of 0.76 and a critical success index of 0.61 with respect to 197 independent
27 rain gauges in the TP, demonstrating that this dataset is remarkably better than the widely-used datasets,
28 including the latest generation of reanalysis (ERA5_land), the state of the art satellite-based dataset
29 (IMERG), and the multi-source merging datasets (MSWEP V2 and AERA5-Asia). Moreover, the TPHiPr
30 can better detect precipitation extremes compared with these widely-used datasets. Overall, this study
31 provides a new precipitation dataset with high accuracy for the TP, which may have broad applications
32 in meteorological, hydrological and ecological studies. The produced dataset can be accessed via
33 <https://doi.org/10.11888/Atmos.tpsc.272763> (Yang and Jiang, 2022).

34 **Keywords:** Third Pole region, Precipitation, High-density rain gauges, Atmospheric simulation, Merging
35

36 **1. Introduction**

37 The Third Pole (TP) region is one of the most complex-terrain regions with high elevations and
38 heterogeneous land surfaces, and strong water and energy exchanges between land surface and
39 atmosphere exist in this region (Chen et al., 2021). Moreover, it is the source of many large Asian rivers,
40 providing abundant water resources and hydropower within and beyond this region (Yao et al., 2022).
41 Meanwhile, the TP suffers from frequent natural hazards (e.g. flash floods, debris flows, landslides),
42 especially in the periphery of the TP (Cui and Jia, 2015). Reliable gridded precipitation data is essential
43 for understanding hydrological processes, planning water resources and preventing natural hazards in the
44 TP (Gao et al., 2021; Wang et al., 2018).

45 At present, quasi-global and regional precipitation datasets, including gauge-based products, satellite-
46 based products and reanalysis products, have played an important role over the TP. These datasets include
47 the Asian Precipitation-Highly-Resolved Observational Data Integration Towards Evaluation
48 (APHRODITE; Yatagai et al., 2012), the Integrated Multi-satellitE Retrievals for Global Precipitation
49 Measurement (IMERG; Huffman et al., 2019), the TRMM Multisatellite Precipitation Analysis (TMPA;
50 Huffman et al., 2007), the China Meteorological Forcing Dataset (CMFD; He et al., 2020), the fifth
51 generation ECMWF atmospheric reanalysis (ERA5; Hersbach et al., 2020) and its downscaled version
52 for land applications (ERA5_land; Muñoz-Sabater et al., 2021) , the High Asia Refined analysis (HAR;
53 Maussion et al., 2014) and its version 2 (HAR V2; X. Wang et al., 2020), et al. Among these products,
54 gauge-based products may have large errors in the TP, since they are mostly interpolated based on sparse
55 gauge observations. Satellite or satellite-gauge combined products are most widely used in the TP.
56 However, they are proven to misrepresent solid precipitation and orographic precipitation, and show
57 large uncertainties in winter and in the western and southeastern TP (Gao et al., 2020; Lu and Yong, 2018;
58 Xu et al., 2017). Atmospheric simulation with fine spatial resolution can give reasonable atmospheric
59 water transport and precipitation spatial variability in complex terrain (Curio et al., 2015; Maussion et
60 al., 2014; Norris et al., 2017; Ouyang et al., 2021; Sugimoto et al., 2021; Wang et al., 2020b; Zhou et al.,
61 2021), moreover, it is skillful in estimating solid precipitation (Lundquist et al., 2019; Maussion et al.,
62 2014). However, current atmospheric simulation-based datasets consistently overestimate precipitation
63 amount in the TP (Gao et al., 2015; Wang et al., 2020b; Zhou et al., 2021). As a result, substantial

64 differences exist among these datasets in the TP in terms of both amount and spatial variability of
65 precipitation (D. Li et al., 2020; Lu and Yong, 2018; Tan et al., 2020; Wang and Zeng, 2012; You et al.,
66 2012). In addition, these datasets typically have a horizontal resolution coarser than 10 km, which is
67 insufficient to represent the fine-scale precipitation variability and cannot be applied locally.

68 Errors in precipitation products hinder the correct understanding of water cycle processes in the TP. For
69 example, Immerzeel et al. (2015) found that the simulated runoff in the upper Indus using APHRODITE
70 is much smaller than the observations and further confirmed that APHRODITE severely underestimates
71 precipitation amount in this region. Savéan et al. (2015) pointed out that precipitation from rain gauges
72 with poor spatial representativeness leads to irrational runoff component simulations in the central
73 Himalayas. Jiang et al. (2022) demonstrated that currently widely-used satellite-based precipitation
74 products cannot close the basin-scale water budget in the eastern edge of the TP. Some other studies also
75 demonstrated the high uncertainties in current precipitation products for simulations of snow cover (Gao
76 et al., 2020), soil moisture (Yang et al., 2020) and river discharge (Alazzy et al., 2017).

77 Merging multiple precipitation products is an effective way to mitigate precipitation uncertainties. The
78 most commonly used strategy for improving the accuracy of satellite or modeling precipitation is bias
79 correction with gauge observation-based data. For example, Shen et al. (2014) combined the probability
80 density matching and the optimal interpolation to merge the CMORPH and rain gauge data and produced
81 a high-accuracy precipitation dataset over China. Ma et al. (2020, 2022) produced the AIMERG and
82 AERA5-Asia datasets by correcting the bias of IMERG and ERA5_land using precipitation from the
83 APHRODITE, respectively. Another strategy is merging multiple precipitation products by assigning
84 different weights to these products, in which the weights can be determined by Bayesian-based methods
85 (Li et al., 2021; Ma et al., 2018), machine learning or the inverse of errors against gauge data (Hong et
86 al., 2021; Zhu et al., 2022). These methods are flexible and able to integrate information from multiple
87 sources. Recently, many efforts have been made to merge different precipitation products over the TP,
88 e.g. Li et al. (2021) produced a high-accuracy precipitation dataset for the southern TP by merging three
89 satellite-based precipitation datasets with high-density rain gauge data. Wang et al. (2020a) developed a
90 long-term precipitation dataset for the Yarlung Tsangpo River basin by merging data from satellites,
91 reanalysis and rain gauges. Although encouraging progresses have been made, there are still some
92 limitations. First, these works either corrected gridded precipitation with data from sparse rain gauge

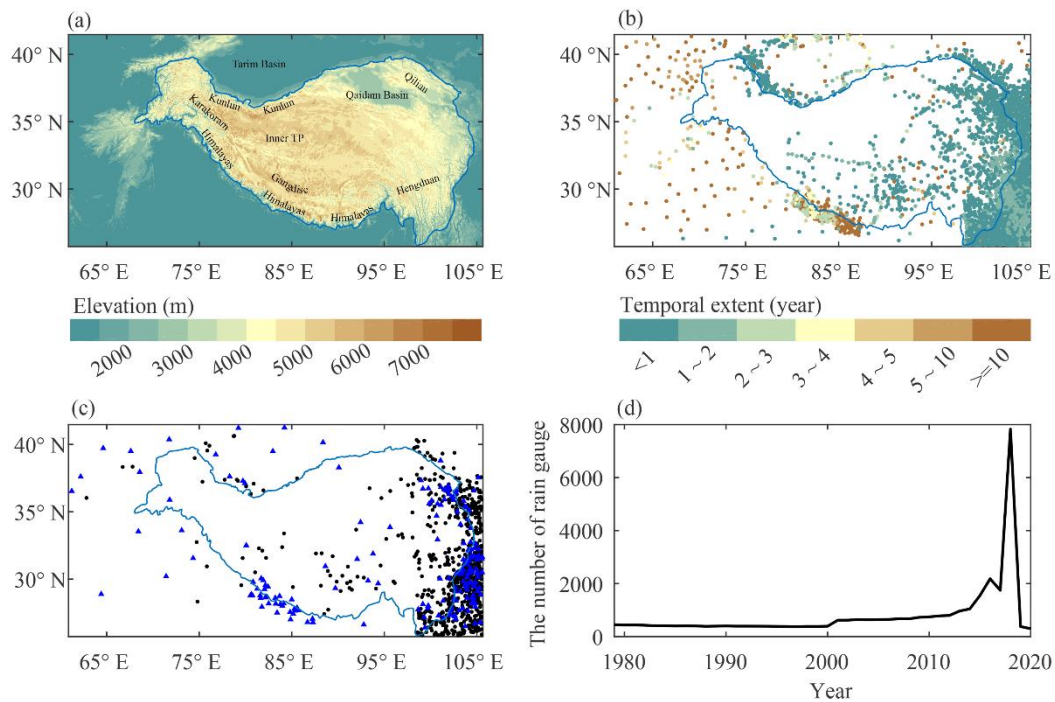
93 networks or were conducted in sub-regions of the TP. Second, most works have merged satellite products
94 with rain gauge data, while both the two sources of precipitation perform poorly in reflecting
95 heterogeneous precipitation in complex terrain. Therefore, substantial improvements are still needed for
96 producing high-accuracy precipitation data in the TP.

97 Therefore, the main goal of this study is to produce a long-term high-resolution precipitation dataset with
98 high accuracy for the TP, by merging dense rain gauge data with high-resolution atmospheric simulation-
99 based precipitation. Different from many previous works that usually merged satellite datasets with rain
100 gauge data, our study uses an atmospheric simulation-based precipitation with very high horizontal
101 resolution ($1/30^\circ$) as the background field, mainly due to its advanced skill in giving the spatial variability
102 of precipitation in complex terrain, which is especially important in high mountains and the western TP.
103 In addition, we collected observations from more than 9000 rain gauges to generate the merged data,
104 including observations from rain gauges in the central and western TP that are set up by this study. To
105 the best of our knowledge, such a gauge density is the highest among the works of precipitation merging
106 over the TP that usually used a portion of data from the CMA (China Meteorological Administration) or
107 MWR (Ministry of Water Resources in China) stations that are mainly distributed in the eastern TP.

108 **2. Data**

109 **2.1 Rain gauge data**

110 Rain gauge data used in this study are obtained from several sources, including the CMA, the MWR, the
111 Department of Hydrology and Meteorology of Nepal (DHM), the Global Historical Climatology
112 Network (GHCN; Menne et al., 2012), and some other field observation networks (Chen et al., 2014,
113 2015; Luo, 2018; Wei and Wang, 2019; Wang, 2021; Yang, 2018; Yang et al., 2017; Zhang, 2018; Zhao,
114 2018; Zhao et al., 2017). These networks provide either daily or sub-daily precipitation records. In
115 addition, our group has set up more than 80 rain gauges over the TP since 2017, deployed in the Yadong
116 Valley, the south slope of Gangdise Range, the eastern edge of the TP, the surroundings of the Namco
117 Lake and the Inner TP. These rain gauges record precipitation every hour and observations from this
118 network are also used in this study. All the sub-daily records are aggregated into daily sum, so that they
119 can be merged with gridded data at a daily scale.



120

121 **Figure 1:** (a) Topography of the Third Pole region. (b) Spatial distribution of rain gauges used in this
 122 study and their temporal extent. (c) The independent rain gauges used for validation, in which rain gauges
 123 marked by both black dot and blue triangle are used in the analysis period of 1979-2020 (section 4.1.2),
 124 and rain gauges marked by blue triangles are used in the analysis period of 2008-2015 (section 4.2). (d)
 125 The number of available rain gauges in each year. The blue line denotes the 2500 m contour of elevation,
 126 which is obtained from Zhang (2019).

127 A series of quality control procedures are applied to the rain gauge data following the method of Hamada
 128 et al. (2011), including outlier check, repetition check, and spatial consistency check. Detailed judgment
 129 criteria for each check can refer to Hamada et al. (2011). In addition, for each rain gauge, data records
 130 for a certain year less than 60 days are removed since they are likely to suffer from a technical broken.
 131 After the quality control, data from 9798 rain gauges are eventually selected for precipitation merging
 132 and these data have temporal coverages ranging from a few months to more than 40 years. Figure 1b
 133 shows the spatial distribution and temporal extent of these rain gauges and Fig. 1d gives the number of
 134 available rain gauges in each year.

135 Rain gauge observations usually suffer from measurement errors, including wind-induced undercatch,
 136 wet loss and evaporation loss. This especially happens in the TP where the wind is strong and solid
 137 precipitation accounts for a large proportion of the total precipitation. Therefore, the measurement errors

138 are corrected in this study. For gauges where observed wind speed and air temperature are provided, the
139 empirical relationships provided by Ye et al. (2007) and Ma et al. (2015) are used to correct the
140 measurements. For gauges without wind speed and air temperature observations, the Random Forest (RF;
141 Breiman, 2001) model is used to correct precipitation. This is achieved with the following steps: first,
142 the RF model is trained at the above-corrected gauges, using wind speed and air temperature from ERA5
143 and original observed daily precipitation as model input and the corrected precipitation as the target; then,
144 the trained model is applied to gauges without wind speed and air temperature observations to estimate
145 corrected precipitation, using wind speed and air temperature from ERA5. The ERA5 is used here mainly
146 because our evaluation with gauge observations showed that ERA5 could give reliable wind speed and
147 air temperature estimates over the TP, as well as reported by Huai et al. (2021) who demonstrated that
148 ERA5 is superior to other global reanalysis datasets for most near-surface meteorological variables in
149 the northeastern TP.

150 **2.2 Gridded precipitation dataset**

151 The background precipitation dataset used in this study is called ERA5_CNN, an atmospheric
152 simulation-based dataset, derived from combing a short-term high-resolution WRF simulation (Zhou et
153 al., 2021) with ERA5 reanalysis. More specifically, a two-year high-resolution WRF simulation is first
154 obtained and used for training a convolutional neural network (CNN)-based downscaling model. Then,
155 the trained model is used to downscale the long-term ERA5 precipitation to generate the ERA5_CNN
156 (Jiang et al., 2021). The ERA5_CNN has a daily temporal resolution, covering the period from 1979 to
157 2020. Compared with ERA5, the ERA5_CNN has a higher horizontal resolution of $1/30^\circ$ and smaller
158 wet biases over the TP. Our previous evaluations showed that the ERA5_CNN can give fine-scale spatial
159 variability of precipitation over the complex-terrain TP with high spatial correlations with rain gauge
160 data. Moreover, the ERA5_CNN is more skillful in reproducing the elevation dependence of precipitation
161 in the TP than the coarse HAR V2 and the satellite-based IMERG (Jiang et al., 2022). However, the
162 ERA5_CNN still overestimates precipitation in the TP, which is inherited from atmospheric simulation
163 (Jiang et al., 2021). Therefore, its accuracy needs to be further improved by merging it with high-density
164 gauge observations.

165 For comparison, three widely-used global precipitation datasets, including ERA5_land (hereafter

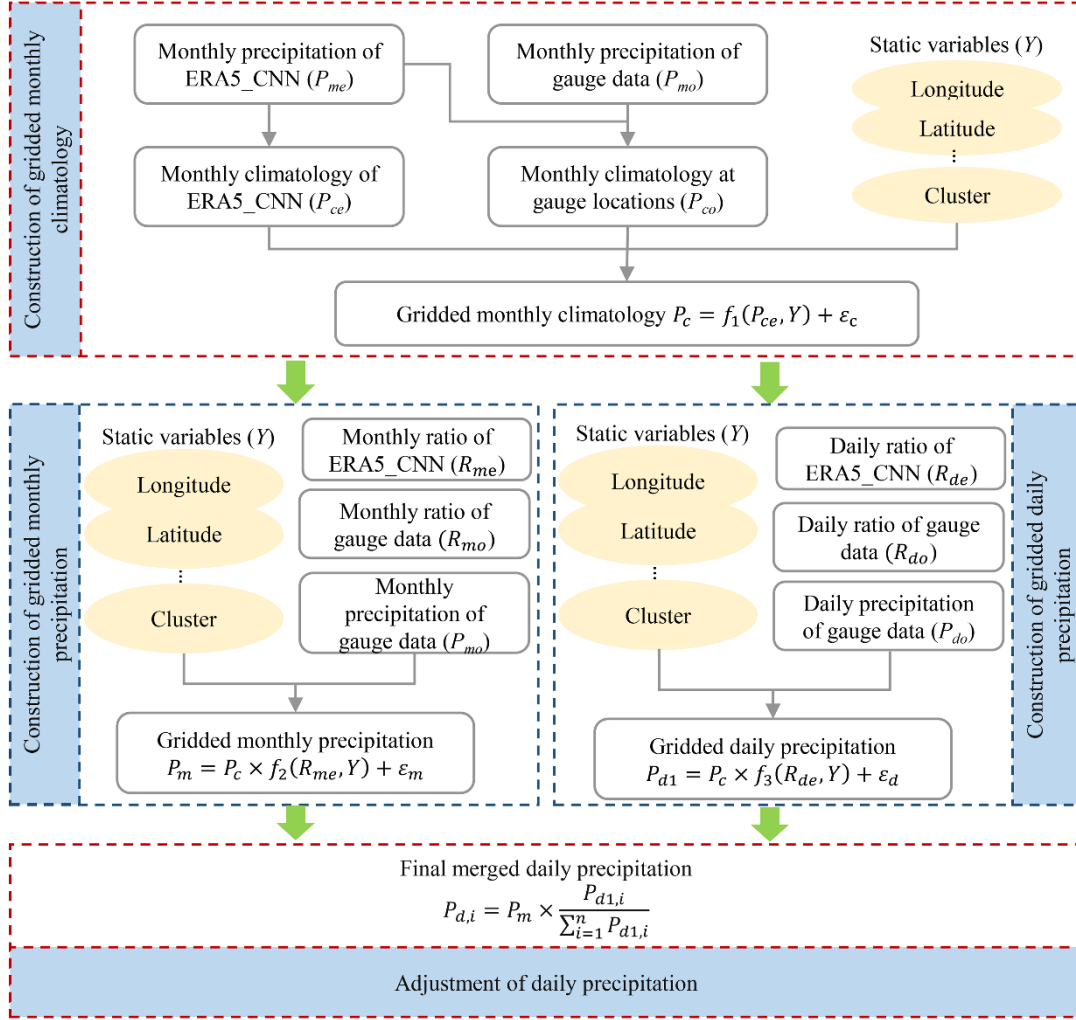
166 ERA5L), IMERG and the Multi-Source Weighted-Ensemble Precipitation version 2 (MSWEP V2; Beck
167 et al., 2019), as well as one regional dataset (AERA5-Asia, hereafter AERA5), are also utilized in this
168 study. The ERA5L is the latest generation reanalysis of the ECMWF for land applications, which
169 provides 0.1 ° precipitation data at 1-hour intervals, compared to 0.25 ° of ERA5. According to Muñoz-
170 Sabater et al. (2021), the precipitation of ERA5L is produced by interpolating the ERA5 with a linear
171 model, thus, the precipitation of ERA5L and ERA5 is slightly different, as shown in the results of Xu et
172 al. (2022). IMERG is a satellite precipitation dataset retrieved from the combination of both microwave
173 and infrared observations and is currently the most widely-used in the world, with a horizontal resolution
174 of 0.1° and the highest temporal resolution of 0.5 hours. The IMERG Final Run V6 (hereafter IMERG),
175 which has been corrected with monthly rain gauge data, is used in this study. The MSWEP V2 with a
176 horizontal resolution of 0.1° is a merged dataset that has combined multiple satellite, gauge, and
177 reanalysis precipitation datasets. Moreover, it is corrected with observed discharge from many
178 catchments worldwide. The AERA5 is a regional precipitation dataset for Asia, which is produced by
179 combining the ERA5L with the APHRODITE dataset. It has a horizontal resolution of 0.1 ° and temporal
180 resolution of 1 hour, covering the period from 1951 to 2015. Previous evaluations showed that the
181 AERA5 has a higher accuracy than ERA5L and IMERG, in terms of several metrics involved in
182 precipitation amounts, events and extremes (Ma et al., 2022).

183 **3. Methods**

184 **3.1 Merging algorithm**

185 **3.1.1 General flowchart**

186 This study merges the ERA5_CNN precipitation with high-density rain gauge data based on the idea of
187 the Climatology Aided Interpolation (CAI; Willmott and Robeson, 1995), in which the anomalies/ratios
188 of meteorological variables are interpolated and then added/multiplied to the climatology, instead of
189 directly interpolating the meteorological variables. The CAI method has been widely applied for gridding
190 precipitation and shown good performance (Contractor et al., 2020; Schamm et al., 2014; Xie et al., 2007).
191 Figure 2 shows the flowchart for merging ERA5_CNN and rain gauge data. The merging procedures
192 include the construction of monthly precipitation climatology, monthly precipitation and daily
193 precipitation. Details are listed below.



194

195 **Figure 2:** General flowchart of the merging algorithm. The static variables include the longitude, latitude,
 196 elevation, standard deviation of elevation and the identifier of the clusters with different precipitation
 197 characteristics. The subscript ‘o’ represents observation, ‘e’ represents ERA5_CNN, ‘c’ represents
 198 climatology, ‘m’ represents monthly, ‘d’ represents daily, ‘n’ represents the number of days in a month
 199 and ‘i’ represents the i th day in a month. $f_1(\bullet)$, $f_2(\bullet)$ and $f_3(\bullet)$ denote the regression models based on
 200 Random Forest. ε_c , ε_m and ε_d represent the residuals of estimations from RF, which are interpolated
 201 using the Kriging method.

202 (1) Construction of monthly precipitation climatology.

203 Since the length of the data records varies from gauge to gauge, it is undesirable to obtain monthly
 204 climatology fields via directly interpolating the observed multi-year average monthly precipitation.
 205 Therefore, we first construct monthly precipitation climatology at gauge locations based on the monthly

206 precipitation climatology of ERA5_CNN, using the following formula:

$$207 \quad P_{co} = P_{ce} \times \frac{P_{co1}}{P_{ce1}}, \quad (1)$$

208 where P_{co} is the constructed monthly precipitation climatology at gauge location, P_{ce} is the monthly
209 precipitation climatology of ERA5_CNN averaged over 1979-2020, P_{co1} is the monthly precipitation of
210 rain gauge averaged over the observing period, which varies from gauge to gauge, and P_{ce1} is the monthly
211 precipitation of ERA5_CNN averaged over the same observing period at the collocated grids.

212 The precipitation climatology fields for the 12 months are then constructed by interpolating the monthly
213 climatology at gauge locations using a RF and Kriging-based method, in which the monthly climatology
214 of ERA5_CNN is taken as an auxiliary and will be introduced in section 3.1.2.

215 (2) Construction of gridded monthly precipitation

216 In this study, the ratios of monthly precipitation to its climatology are adopted for constructing monthly
217 precipitation fields. There are four steps for constructing monthly precipitation fields. First, the ratios of
218 observed monthly precipitation (P_{mo}) to the precipitation climatology (P_{co}) are calculated at gauge
219 locations (i.e. R_{mo} in Fig. 2); second, the ratios are gridded using the RF method by taking the monthly
220 precipitation ratios of ERA5_CNN ($R_{me}=P_{me}/P_{ce}$) and static variables (Y) as auxiliaries; third, the gridded
221 ratios are multiplied by the gridded monthly precipitation climatology (P_c) obtained in step (1) to
222 construct the first guess of gridded monthly precipitation fields; finally, the residuals (ε_m) of the first
223 guess against gauge observations are gridded using the Kriging method and added to the first guess to
224 construct the final monthly precipitation fields (P_m).

225 (3) Construction of gridded daily precipitation

226 The procedures for constructing daily precipitation fields are similar to monthly precipitation, with only
227 two differences. First, the ratios are daily precipitation to monthly climatology (i.e. P_{do}/P_{co} and P_{de}/P_{ce})
228 in this part. Second, the daily precipitation fields after residual correction (P_{dl}) are further adjusted to
229 ensure that the sum of the daily precipitation amount in a month is equal to the corresponding monthly
230 precipitation amount obtained in step (2), given that monthly precipitation fields are more reliable due to
231 their less spatial variability than daily fields (He et al., 2020). The adjustment can be expressed as follow:

232
$$P_{d,i} = P_m \times \frac{P_{d1,i}}{\sum_{i=1}^n P_{d1,i}}, \quad (2)$$

233 Where $P_{d,i}$ is the adjusted precipitation for the i th day in a month, $P_{d1,i}$ is the precipitation after residual
234 correction for the i th day, P_m is the monthly precipitation and n is the number of days in that month.
235 When the monthly precipitation (P_m) is no-zero but the sum ($\sum_{i=1}^n P_{d1,i}$) of the daily precipitation amount
236 in that month is zero, we will search the nearest grid that has a non-zero $\sum_{i=1}^n P_{d1,i}$ and then disaggregate
237 P_m to daily precipitation according to the day-to-day variation of precipitation in the nearest grid.

238 In the above procedures, gridding multiple variables, including the monthly climatology, the ratios of
239 monthly/daily precipitation to monthly climatology and the monthly/daily residuals, is achieved based
240 on the RF and Ordinary Kriging, which will be introduced in section 3.1.2.

241 **3.1.2 Gridding method**

242 Gridding monthly precipitation climatology, precipitation ratio and the residual is the key for merging
243 ERA5_CNN and rain gauge data. In this study, the RF is combined with the Ordinary Kriging to
244 interpolate these variables, which is inspired by the Regression Kriging method, in which the interpolated
245 target is assigned to the spatial trend (deterministic) and the stochastic component (residual). A regression
246 model is applied to predict the spatial trend and the Ordinary Kriging is used to estimate the stochastic
247 component that is expected to be a Gaussian distribution. In this method, various regression methods can
248 be combined with Kriging, including machine learning methods. Machine learning-based regression
249 models combined with Kriging were widely applied in earth science and proved to have good
250 performance, as reported in many previous works (Araki et al., 2015; Cellura et al., 2008; Demyanov et
251 al., 1998). The machine learning method used in this study is the RF model, which is an ensemble
252 machine learning model based on the decision tree algorithm and can learn the complex non-linear
253 relationships between multiple covariates and the target variable. It randomly selects samples for training
254 each Decision Tree and aggregates estimates from multiple Decision Trees. Compared to other machine
255 learning methods, the RF is less sensitive to hyperparameters, less likely to suffer from overfitting and
256 has good generalization capability. Moreover, The RF is easy to implement and has robust prediction
257 accuracy, thus making it a widely-used method for the correction and downscaling of meteorological
258 variables (Baez-Villanueva et al., 2020; He et al., 2016; Sekulić et al., 2021; Zhang et al., 2021). The
259 general formulation for constructing precipitation at multiple timescales based on RF and Kriging can be

260 expressed as follow:

$$261 \quad \begin{cases} P_c = f_1(P_{ce}, Y) + \varepsilon_c, & \text{for monthly precipitation climatology} \\ P_m = P_c \times f_2(R_{me}, Y) + \varepsilon_m & \text{for monthly precipitation} \\ P_{d1} = P_c \times f_3(R_{de}, Y) + \varepsilon_d & \text{for daily precipitation} \end{cases} \quad (3)$$

262 where P_c is the monthly precipitation climatology, P_m and P_{d1} are the monthly and daily precipitation,
263 respectively, f_1, f_2 and f_3 are the non-linear regressive relationships built with the RF model, P_{ce} is the
264 monthly precipitation climatology from ERA5_CNN, R_{me} and R_{de} are the ratio of monthly and daily
265 precipitation to the climatology from ERA5_CNN, respectively, Y is the static variables and $\varepsilon_c, \varepsilon_m$ and ε_d
266 are the residuals of the estimated precipitation.

267 Multiple covariates are used to build the RF model. For gridding monthly precipitation climatology, the
268 target for training the RF model is the monthly precipitation climatology at the gauge locations (P_{co}), and
269 the inputs are monthly precipitation climatology from ERA5_CNN (P_{ce}) at nine grids around the target
270 location, longitude, latitude, elevation and standard deviation of elevation around the target location. In
271 addition, the study area is divided into 25 clusters according to the monthly variation of precipitation and
272 the identifier for the cluster is also input into the RF model. For gridding the ratio of monthly/daily
273 precipitation to monthly climatology, the training target is the observed ratio of monthly/daily
274 precipitation to monthly climatology (R_{mo} or R_{do}), and the inputs are the same as those for gridding
275 precipitation climatology except that the ratios of monthly/daily precipitation to monthly climatology
276 from ERA5_CNN (R_{me} or R_{de}) are input to the model rather than monthly climatology. Model training
277 performs for each month, i.e. samples from all gauges and all years in a month are gathered together and
278 used for model training.

279 In Eq. (3), the residuals are calculated as follows: first, we calculate the differences between the gauge
280 observations (P_{mo} or P_{do}) and the precipitation estimates from RF at gauge locations; Then, the
281 Ordinary Kriging is used to interpolate the differences. The difference fields are added to the precipitation
282 estimates from RF to obtain the final estimates of precipitation.

283 **3.2 Evaluation metrics**

284 Several metrics are used for validating the merged precipitation, including relative bias (Rbias), root
285 mean square error (RMSE), correlation coefficient (CC), probability of detection (POD), false alarm ratio

286 (FAR) and critical success index (CSI). The formulas and perfect values for these metrics are listed in
 287 Table 1. These metrics are calculated at a daily scale by comparing the gauge observations with the
 288 gridded precipitation from the nearest grid to the rain gauge.

289 **Table 1** The error metrics used in this study

Metrics	Formula	Perfect value
Relative bias	$Rbias = \frac{\sum_{i=1}^n (M_i - O_i)}{\sum_{i=1}^n O_i}$	0
Root mean square error	$RMSE = \sqrt{\frac{1}{n} \sum_{i=1}^n (M_i - O_i)^2}$	0
Correlation coefficient	$CC = \frac{\sum_{i=1}^n (M_i - \bar{M})(O_i - \bar{O})}{\sqrt{\sum_{i=1}^n (M_i - \bar{M})^2} \sqrt{\sum_{i=1}^n (O_i - \bar{O})^2}}$	1
Probability of detection	$POD = \frac{H}{H + MM}$	1
False alarm ratio	$FAR = \frac{F}{H + F}$	0
Critical success index	$CSI = \frac{1}{POD^{-1} + (1 - FAR)^{-1} - 1}$	1

290 where n is the number of days, M_i and O_i are the merged and observed precipitation at a specific day,
 291 respectively, \bar{M} and \bar{O} are the mean values of merged and observed precipitation, respectively. H is the
 292 days when both merged data and observation have precipitation. MM is the days when only observation
 293 has detected precipitation. F is the days when only merged data has detected precipitation. For calculating
 294 POD, FAR and CSI, a threshold of 0.1mm day^{-1} is adopted for distinguishing precipitation and non-
 295 precipitation day.

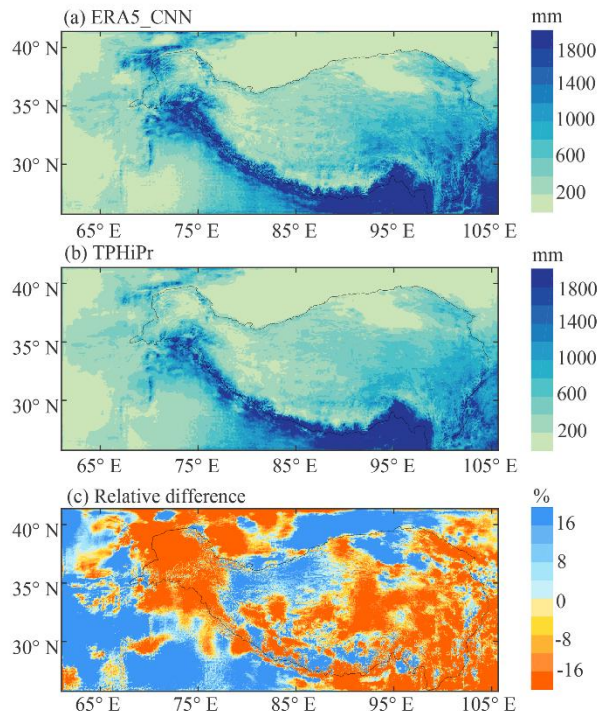
296 4. Results

297 4.1 Validation of the merging algorithm

298 4.1.1 Merging effect on precipitation amount and spatial pattern

299 The spatial patterns of average annual precipitation from ERA5_CNN and the merged data (TPHiPr)
 300 during 1979-2020 are shown in Fig. 3a and b. It can be found that ERA5_CNN and TPHiPr have similar
 301 spatial patterns of precipitation in the TP. Both have large precipitation amounts in the southeast of the
 302 TP and along the Himalayas, while having small precipitation amounts in the Qaidam Basin, the Tarim

303 Basin and the Inner TP. The similar spatial patterns of ERA5_CNN and TPHiPr demonstrate that the
304 merging algorithm generally retains the spatial characteristics of precipitation from ERA5_CNN.



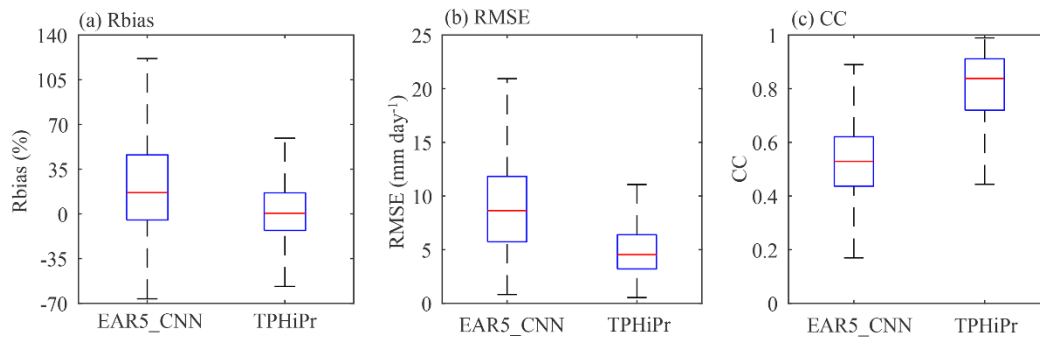
305
306 **Figure 3:** Spatial patterns of the annual average precipitation from (a) ERA5_CNN and (b) the merged
307 data (TPHiPr), as well as (c) the relative difference between them. The precipitation is averaged over the
308 period from 1979 to 2020. The relative difference is calculated by subtracting ERA5_CNN from TPHiPr,
309 and then dividing by ERA5_CNN.

310 The relative difference between ERA5_CNN and TPHiPr is also calculated and shown in Fig. 3c.
311 Generally, by merged with rain gauge data, the precipitation amount is reduced in the TP. The
312 precipitation amount averaged over the study area decreases from 696.4 mm year⁻¹ of ERA5_CNN to
313 600.9 mm year⁻¹ of TPHiPr. This corresponds to previous works that have demonstrated the
314 overestimation in the atmospheric simulation-based precipitation datasets (Gao et al., 2015; Jiang et al.,
315 2021; Wang et al., 2020b; Zhou et al., 2021). Spatially, the precipitation decrease is evident (up to 20%)
316 in the central and eastern TP, the western Himalayas, the Karakoram and the Tarim Basin, while
317 precipitation amount increases in the Qaidam Basin and its north, the southwest of the TP and the eastern
318 Kunlun.

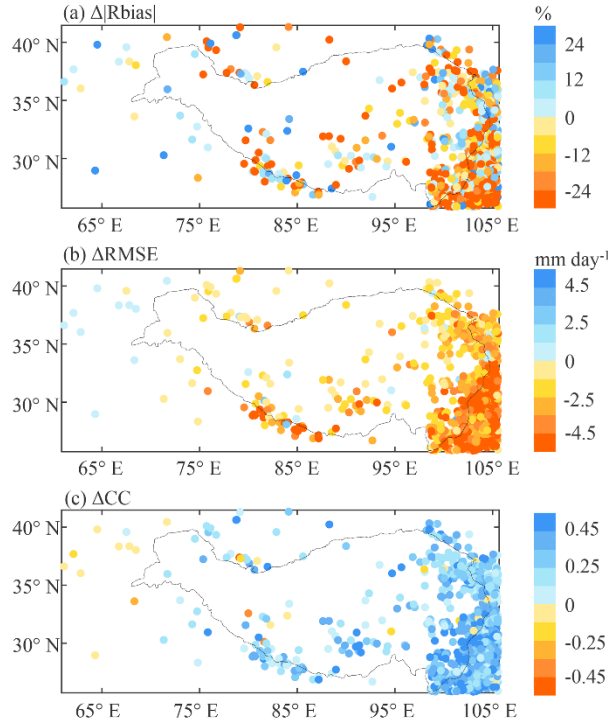
319 4.1.2 Validation with independent gauge data

320 In this study, about 10% of the total rain gauges are randomly excluded for independent validation of
321 TPHiPr, and several metrics against rain gauge data are calculated for ERA5_CNN and TPHiPr at these
322 rain gauges based on daily precipitation.

323 Figure 4 compares the boxplot of these metrics for ERA5_CNN and TPHiPr. TPHiPr has remarkably
324 better performance than the ERA5_CNN. In terms of the Rbias, ERA5_CNN generally overestimates
325 precipitation in the TP, with the median Rbias value for all these rain gauges of 16.6%. In comparison,
326 the overestimation is largely reduced in TPHiPr, which has a median value of 0.5%. Also, TPHiPr shows
327 smaller RMSE values (with a median value of 4.5 mm day⁻¹) than the ERA5_CNN (with a median value
328 of 8.6 mm day⁻¹). Regarding CC, ERA5_CNN has values between 0.40 and 0.60 at most rain gauges (the
329 median value is 0.53), while they are generally larger than 0.70 for TPHiPr with a median value of 0.84,
330 indicating that precipitation from the TPHiPr has highly consistent temporal variations with rain gauge
331 data. In addition, it can be seen that the Rbias (Fig. 4a) and RMSE (Fig. 4b) for TPHiPr are less divergent
332 than those for ERA5_CNN, implying that TPHiPr has more spatially homogeneous accuracy than
333 ERA5_CNN.



334
335 **Figure 4:** Comparison of error metrics for ERA5_CNN and TPHiPr at 966 independent rain gauges. The
336 box represents the distribution of the metrics for all the independent rain gauges in the TP.



337

338 **Figure 5:** Spatial distribution of error metrics differences between ERA5_CNN and TPHiPr. The
 339 differences are calculated by subtracting the metrics of ERA5_CNN from those of TPHiPr.

340 Figure 5 shows the differences in the three metrics between ERA5_CNN and the TPHiPr at each rain
 341 gauge. After the merging, the rain gauges with better Rbias, RMSE and CC account for 68%, 97% and
 342 96% of the total validation rain gauges, respectively. More than 50% of the rain gauges have RMSE
 343 reductions larger than $3.0\ mm\ day^{-1}$ and about 67% of the rain gauges have CC improved by more than
 344 0.2. Moreover, obvious improvements can be found at many east rain gauges. In the western region,
 345 improvements can also be found at many rain gauges in the high elevations, while the metrics change
 346 little at some rain gauges outside the 2500 m contour.

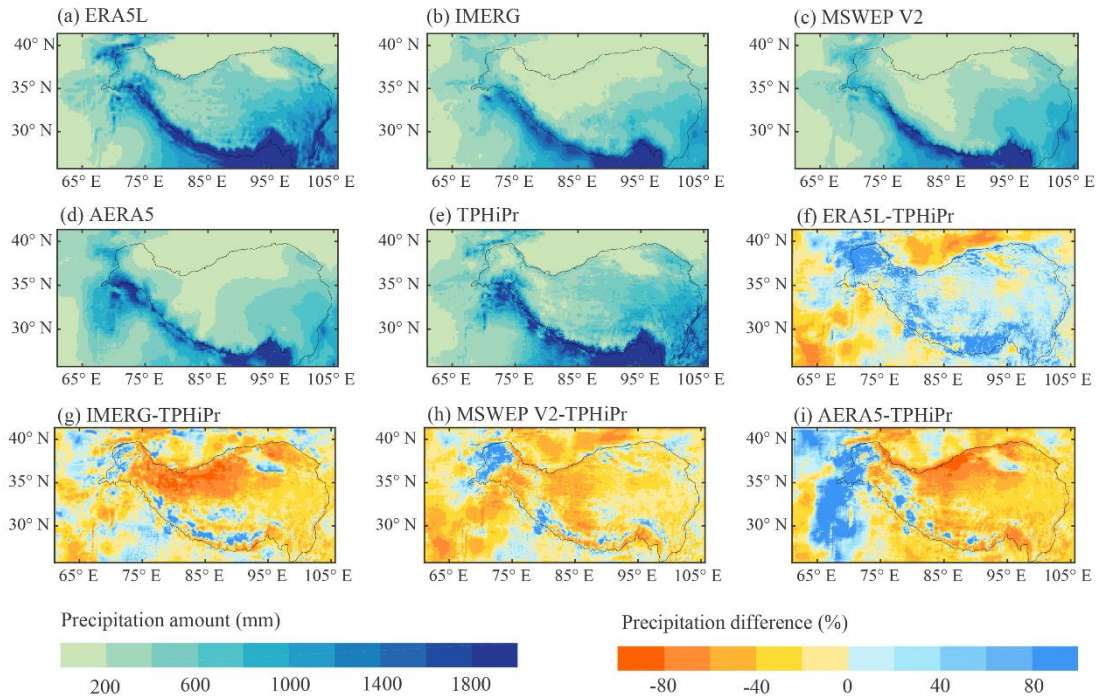
347 In summary, by merged with rain gauge data, the accuracy of ERA5_CNN is well improved in the TP,
 348 especially in regions where high-density rain gauges are located.

349 **4.2 Comparison with other datasets**

350 We also compare the merged precipitation data with other widely-used precipitation products. The
 351 comparison focuses mainly on three aspects: the amount and spatial patterns of precipitation, the error
 352 metrics against rain gauge data and the ability to reproduce precipitation extremes. Because the AERA5
 353 dataset is only available before 2015, the comparison between these datasets is conducted for the period

354 from 2008 to 2015.

355 4.2.1 Precipitation amount and spatial patterns



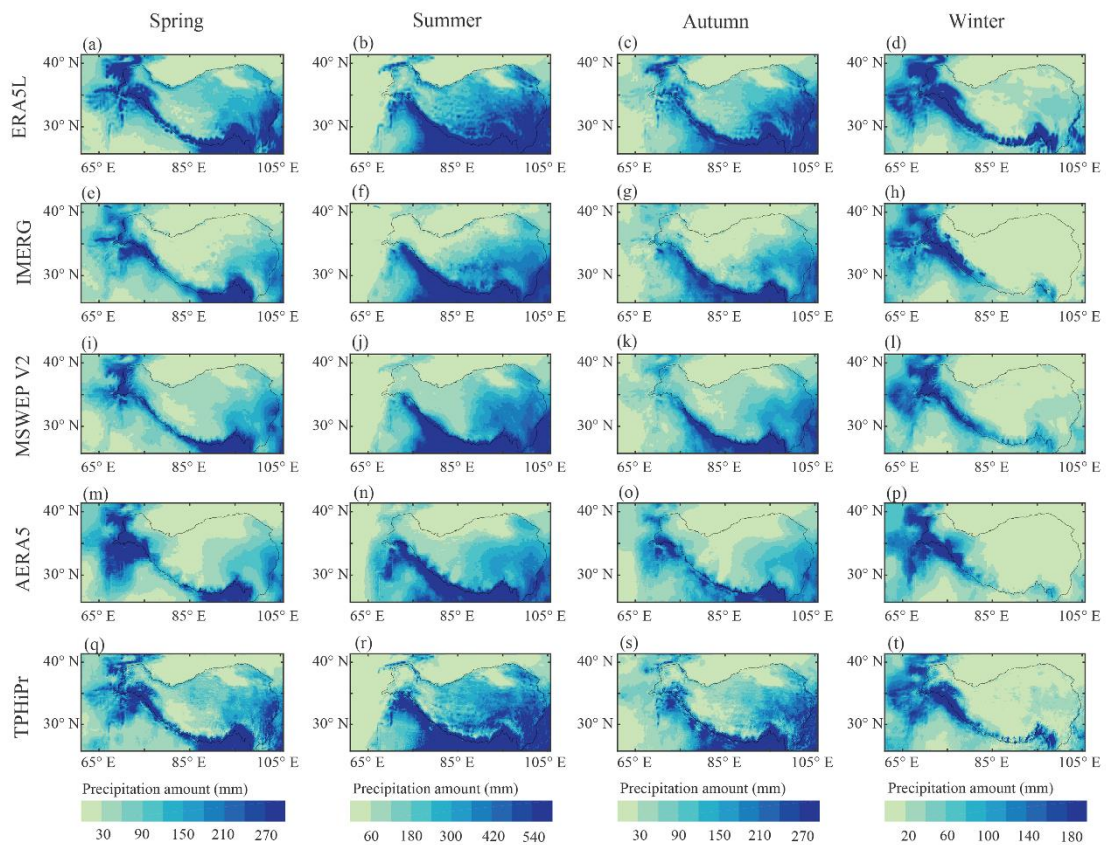
356

357 **Figure 6:** Spatial patterns of (a-e) the average annual precipitation during 2008-2015 from the five
358 datasets and (f-i) the relative differences between TPHiPr and the other four datasets. The differences are
359 calculated by subtracting TPHiPr from the other four datasets and then dividing by TPHiPr.

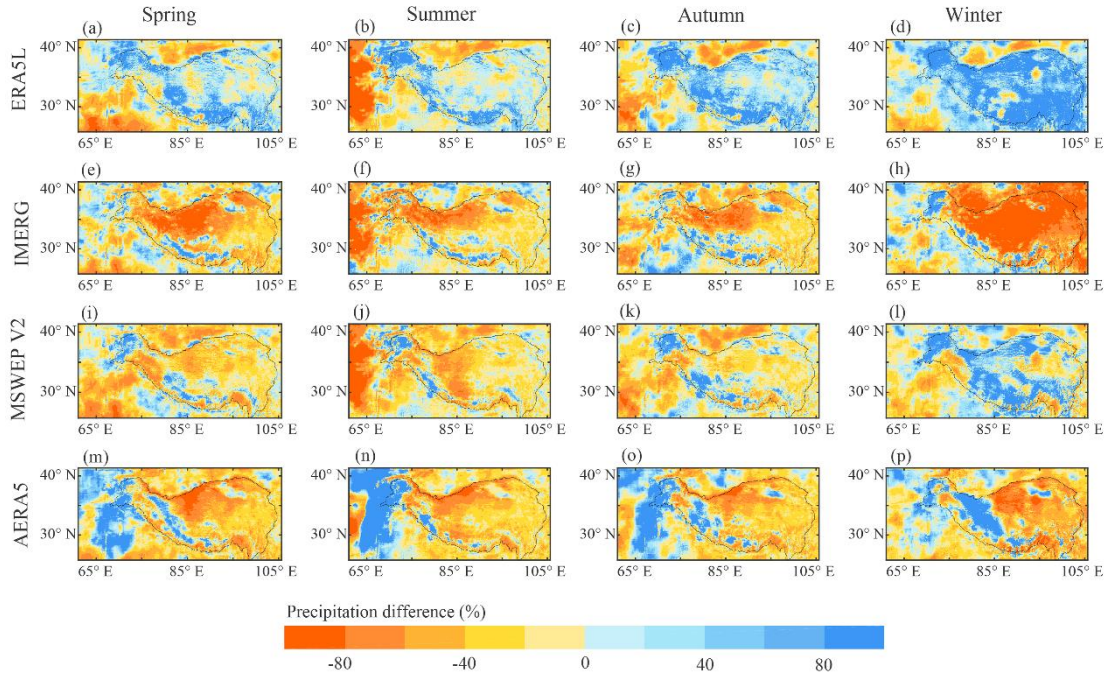
360 Figure 6 shows the spatial patterns of the average annual precipitation during 2008-2015 from the five
361 precipitation datasets, along with the relative differences between TPHiPr and the other four datasets.

362 For calculating the differences between them, the coarser datasets are first resampled to the same
363 horizontal resolution of TPHiPr using bilinear interpolation. Generally, the average annual precipitation
364 (Fig. 6a-6e) from all four datasets decreases from the southeast to the northwest because the monsoon
365 has brought abundant water vapor to the southeastern region of the study area while its impact is reduced
366 in the northwest. In addition, high mountains along the Himalayas block the northward moisture and
367 result in large precipitation amounts in this region, which is revealed by all these datasets. As shown in
368 Fig. 6a-6e, precipitation from IMERG, MSWEP V2 and AERA5 varies more smoothly in space than that
369 from TPHiPr and ERA5L. Moreover, compared with ERA5L, TPHiPr presents more details related to
370 local topography. For example, the dry belt in the northern slope of the central Himalayas (around 90°E,

371 29°N), which was proved in the results of Wang et al. (2019), is more evident in TPHiPr than in ERA5L.
 372 Besides, TPHiPr shows greater spatial variability of precipitation than ERA5L in the Hengduan
 373 Mountains where the topography is much complex with many large mountain ranges and valleys. In
 374 terms of the total precipitation amounts, as shown in Fig. 6f-6i, the ERA5L generally has larger
 375 precipitation amounts than TPHiPr, while the opposite is true for the other three datasets. The
 376 precipitation amounts averaged over the study area from ERA5L, IMERG, MSWEP V2, AERA5 and
 377 TPHiPr are 712.72 mm, 490.50 mm, 496.79 mm, 481.74 mm and 614.11 mm, respectively. Particularly,
 378 it can be noted from Fig. 6f-6i that the differences between these datasets are relatively small in the
 379 eastern TP but are remarkable in the south of the Kunlun mountains (around 85°E, 35°N) where almost
 380 no rain gauges are located, highlighting the high uncertainties of precipitation in ungauged regions.



381
 382 **Figure 7:** Spatial patterns of average seasonal precipitation from ERA5L (first row), IMERG (second
 383 row), MSWEP V2 (third row), AERA5 (fourth row) and TPHiPr (fifth row). The precipitation is averaged
 384 over the period from 2008 to 2015.



385

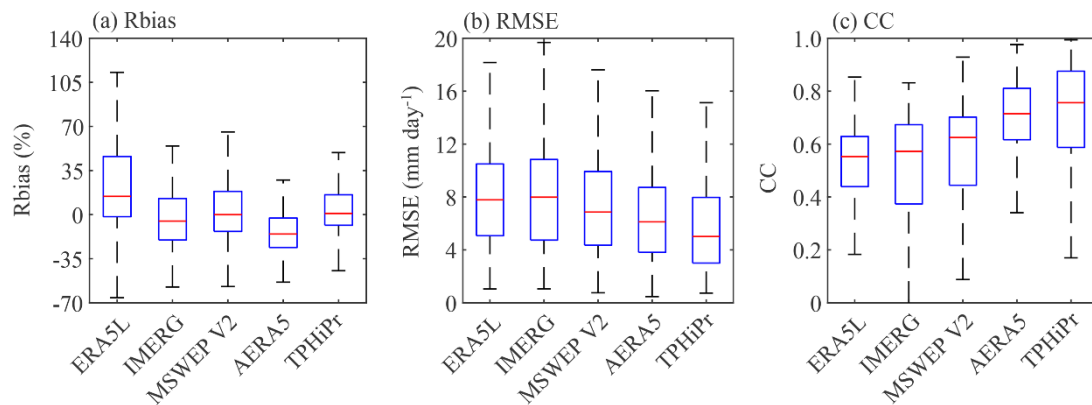
386 **Figure 8:** Spatial patterns of the relative differences in average seasonal precipitation between TPHiPr
 387 and the other four datasets. The differences are calculated by subtracting TPHiPr from the other four
 388 datasets and then dividing by TPHiPr.

389 With respect to the seasonal variations of precipitation, affected by the monsoon climate, most parts of
 390 the TP have large precipitation in summer but small precipitation in winter. In the westerly-dominant
 391 western TP, the precipitation is large in spring and winter but small in summer. All these datasets can
 392 generally capture the seasonal cycles of precipitation in the TP (Fig. 7). The precipitation differences
 393 among these datasets in spring, summer and autumn are generally similar to those of annual precipitation,
 394 with ERA5L having a larger precipitation amount than the TPHiPr but the other three datasets having
 395 smaller. Apparent differences between these datasets occur in winter (fourth column in Fig. 8), in which
 396 the relative differences between ERA5L and TPHiPr are larger than 80% in most regions while most
 397 regions have the relative differences between IMERG and TPHiPr less than -80%. The large differences
 398 in winter likely ascribe to solid precipitation which is challenging for current precipitation datasets,
 399 especially for satellite-based datasets (D. Li et al., 2020; Lu and Yong, 2018).

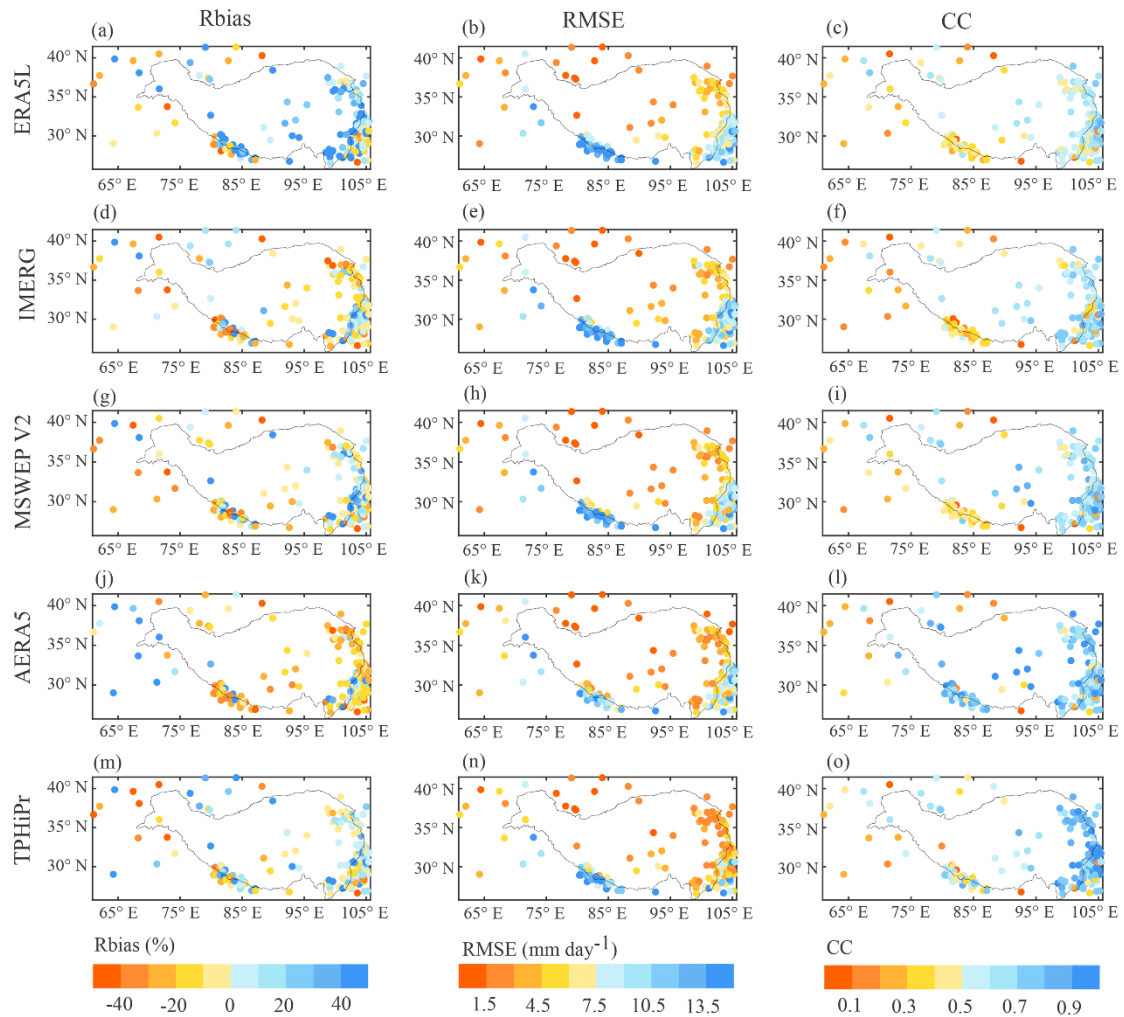
400 4.2.2 Comparison of error metrics

401 The performance of the four widely-used datasets is evaluated with the rain gauge data used for
 402 independent validation in section 4.1.2 and compared with that of TPHiPr in this study. Note that the

403 evaluation in this section span a shorter period from 2008 to 2015 considering the availability of the
 404 AERA5 data and there are only 197 independent rain gauges (blue triangles in Fig. 1c) during this period.
 405 Figure 9 compares the boxplots of the Rbias, RMSE and CC of the five datasets. In terms of the Rbias
 406 (Fig. 9a and the first column in Fig. 10), ERA5L overestimates precipitation at most rain gauges in the
 407 TP with a median value of 14.5% while AERA5 underestimates precipitation with a median value of -
 408 15.4%. The other three datasets generally have small relative biases and the median values for IMERG,
 409 MSWEP V2 and TPHiPr are -5.1%, -0.0% and 0.9%, respectively. For RMSE (Fig. 9b and the second
 410 column in Fig. 10), the three global/quasi-global datasets have relatively large RMSE values in the TP,
 411 with the median value of 7.8 mm day⁻¹ for ERA5L, 8.0 mm day⁻¹ for IMERG and 6.9 mm day⁻¹ for
 412 MSWEP V2. By merged with the APHRODITE, the AERA5 has a well-improved accuracy in the TP
 413 compared to the original ERA5L dataset, with a median RMSE value of 6.1 mm day⁻¹. The TPHiPr has
 414 a median RMSE value of 5.0 mm day⁻¹, which is remarkably smaller than those of the other datasets.
 415 Particularly, the TPHiPr and AERA5 have remarkably higher correlations with rain gauge data compared
 416 to the other three datasets, with more than 70% of the rain gauges having CC value larger than 0.6 (Fig.
 417 9c and the third column in Fig. 10). The median values of CC for TPHiPr and AERA5 are 0.76 and 0.71,
 418 respectively, followed by MSWEP V2 (0.63) and IMERG (0.57). The ERA5L has the lowest correlations
 419 with rain gauge data, with CC values between 0.30 and 0.60 at most gauges and a median value of 0.55.



420
 421 **Figure 9:** Comparison of (a) Rbias, (b) RMSE and (c) CC for ERA5L, IMERG, MSWEP V2, AERA5
 422 and TPHiPr. The box represents the distribution of the metrics for all the 197 independent rain gauges in
 423 the TP.

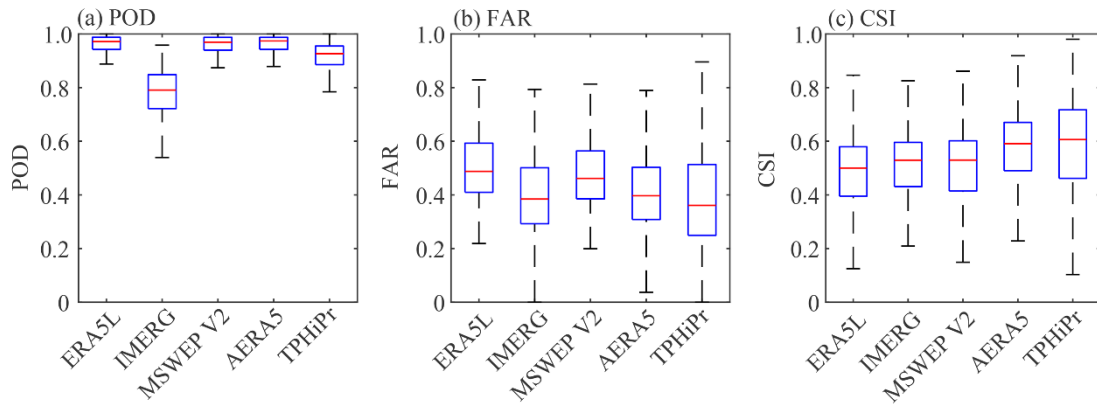


424

425 **Figure 10:** Spatial distribution of Rbias (first column), RMSE (second column) and CC (third column)
 426 for (a-c) ERA5L, (d-f) IMERG, (g-i) MSWEP V2, (j-l) AERA5 and (m-o) TPHiPr. The metrics are
 427 calculated at daily scale.

428 This study also calculates the POD, FAR and CSI for these datasets to compare their performance in
 429 detecting precipitation occurrence. In this section, a threshold of 0.1 mm day^{-1} is used to distinguish rain
 430 and no-rain days. Figure 11 compares the boxplots of these metrics for these datasets, and the spatial
 431 distributions for these metrics are shown in Fig. 12. Among the five datasets, the ERA5L, MSWEP V2
 432 and AERA5 have high values of POD (all have a median value of 0.97). However, it can be seen from
 433 Fig. 11b and Fig. 12 that ERA5L and MSWEP V2 also have large FAR values. This is mainly because
 434 ERA5L is atmospheric reanalysis that tends to overestimate precipitation frequency in the TP (Hu and
 435 Yuan, 2021) while the MSWEP V2 is produced by weighted averaging multiple datasets, which can also
 436 increase the precipitation occurrence. However, AERA5 shows relatively low FAR values, mainly

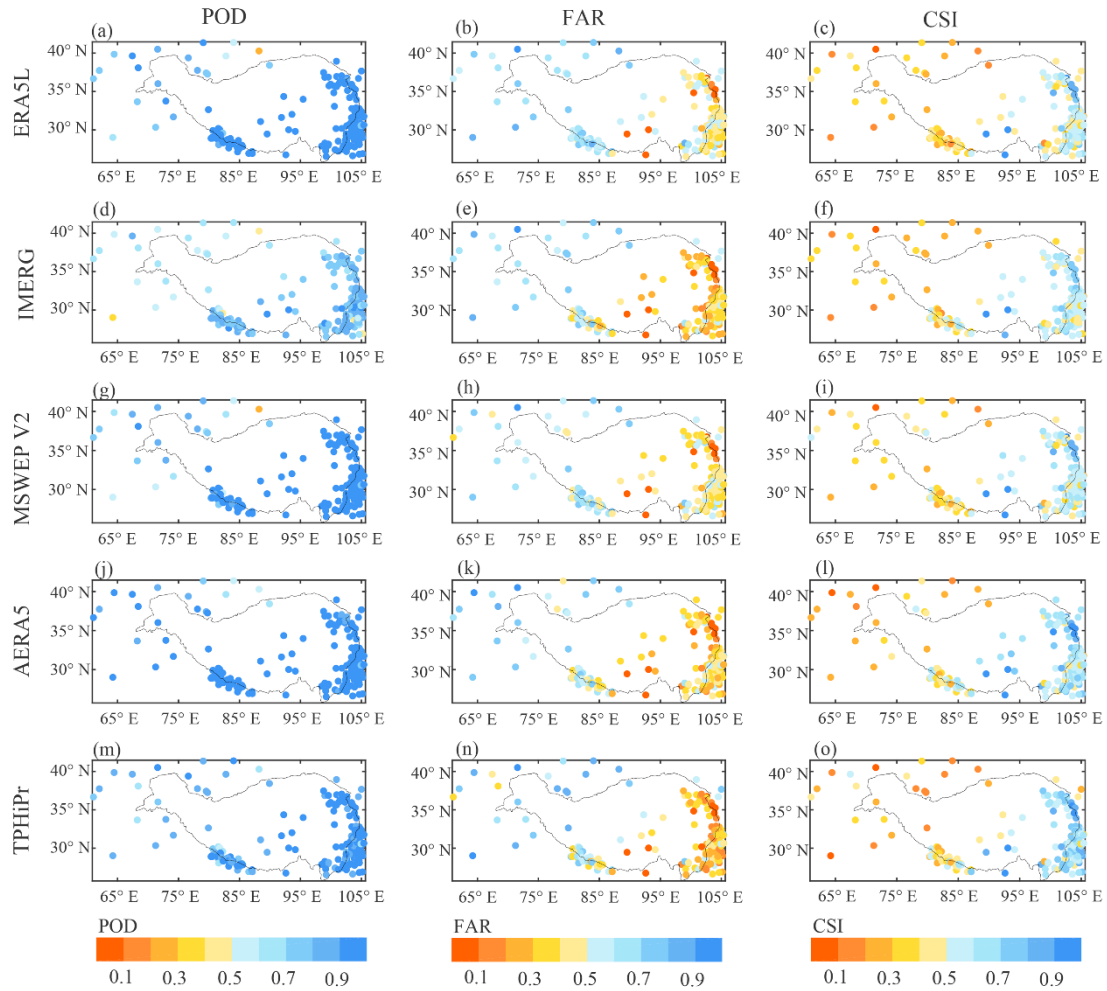
437 ascribing to the correction with gauge data at a daily scale. In contrast, IMERG, mainly based on satellite
 438 estimates, has lower values of POD and FAR. With respect to TPHiPr, Fig. 11 shows that it has relatively
 439 high POD values (the median value is 0.93) and the lowest FAR (the median value is 0.36). As a result,
 440 TPHiPr gains high CSI values, with a median value of 0.61 that is close to AERA5 (0.59), while the other
 441 three datasets have a median CSI value of about 0.50.



442

443 **Figure 11:** Similar to Fig. 9 but for (a) POD, (b) FAR and (c) CSI. These metrics are calculated using a

444 threshold of 0.1 mm day⁻¹.



445

446 **Figure 12:** Similar to Fig. 10 but for POD (first column), FAR (second column) and CSI (third column).

447

In summary, the comparison of these error metrics shows that TPHiPr generally has better performance
 448 than the widely-used reanalysis data (ERA5L), satellite-based data (IMERG), and even performs better
 449 than the multiple-sources merged data (MSWEP V2) and AERA5. In addition, it should be noted that
 450 some validation data from CMA, DHM and GHCN have been used to produce IMERG, MSWEP V2 and
 451 AERA5. Therefore, if these data are removed from the validation, more evident superiority of TPHiPr is
 452 expected.

453

4.2.3 Comparison of precipitation extremes

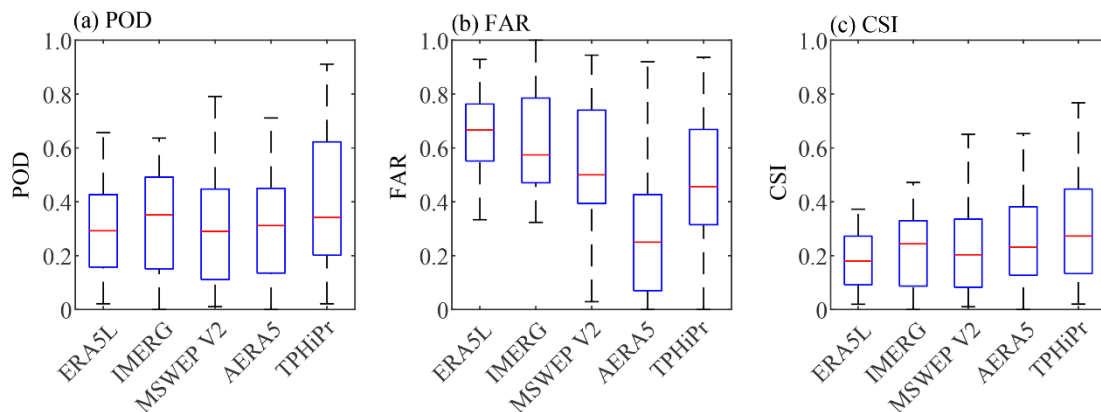
454

Extreme precipitation is the leading cause of many water-related disasters. Therefore, this study also
 455 evaluates the performance of TPHiPr to reproduce extreme precipitation. Following some previous works
 456 (Katsanos et al., 2016; Li et al., 2022; Lockhoff et al., 2014), the 90th percentile of daily precipitation on
 457 wet days is set as the threshold for extreme precipitation in this study. Due to discontinuous temporal

458 coverages of gauge observations, this study only evaluates the extreme precipitation of these datasets at
459 91 rain gauges with at least 2-year precipitation records and covering a complete seasonal cycle.

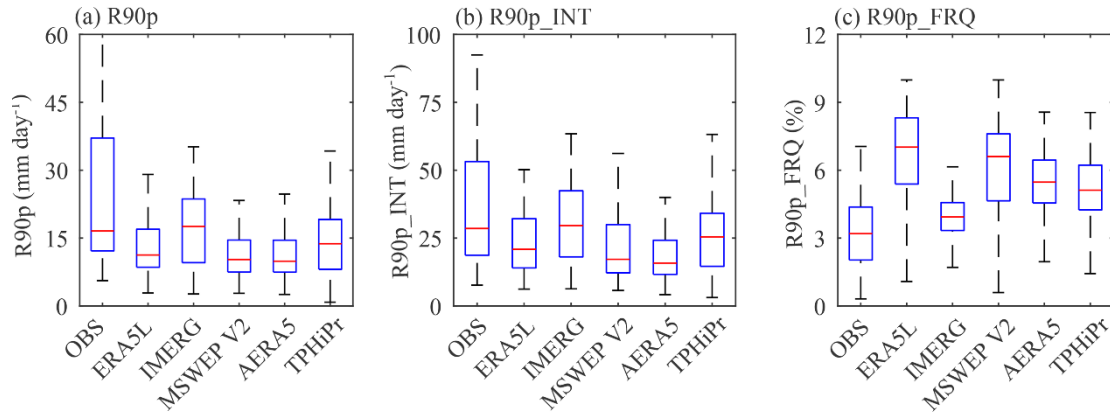
460 Figure 13 compares the detection skill of these precipitation datasets for extreme precipitation. Compared
461 with the detection skill for all precipitation events (Fig. 11), the detection skill of all the datasets for
462 extreme precipitation is obviously reduced, with lower POD and CSI but higher FAR. Nevertheless,
463 TPHiPr also shows good performance. The median value of CSI for TPHiPr is 0.27, which is the highest
464 among these datasets.

465 The 90th percentile (R90p) of daily precipitation on wet days, the average intensity (R90p_INT) and the
466 frequency (R90p_FRQ) of precipitation greater than R90p are also calculated for each dataset and
467 compared with those of rain gauge data. Figure 14 shows that all these datasets have smaller R90p and
468 R90p_INT but higher R90p_FRQ compared to the gauge data, indicating all these datasets underestimate
469 the intensity but overestimate the frequency of extreme precipitation. TPHiPr has a worse performance
470 than IMERG, however, it performs better than the other three datasets.



471

472 **Figure 13:** Similar to Fig. 11, but for extreme precipitation. The 90th percentile of observed daily
473 precipitation at each rain gauge is taken as the threshold for calculating these metrics.



474

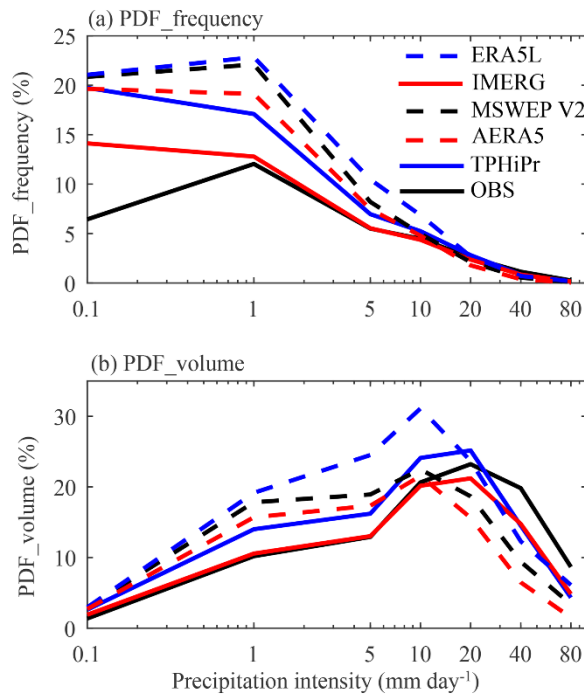
475 **Figure 14:** Comparison of (a) R90p, (b) R90p_INT and (c) R90p_FRQ for rain gauge data (OBS),
 476 ERA5L, IMERG, MSWEP V2, AERA5 and TPHiPr. R90p represents the 90th percentile of daily
 477 precipitation on wet days for each dataset. R90p_INT represents the average precipitation intensity of
 478 daily precipitation larger than R90p. R90p_FRQ represents the frequency of daily precipitation larger
 479 than R90p.

480 In summary, although the TPHiPr underestimates the intensity but overestimates the frequency of
 481 extreme precipitation, it has better performance than the other four datasets in detecting the occurrence
 482 of extreme precipitation.

483 5. Limitations

484 The above analysis shows that the TPHiPr produced in this study generally has high accuracy in the TP
 485 and is superior to the most widely-used precipitation datasets. However, there are still some limitations
 486 in TPHiPr that need to be clarified.

487 As shown in Fig. 5, by merged with the rain gauge data, the accuracy of the gridded data is generally
 488 improved, but the improvements vary greatly in space. In the eastern TP, the improvement is evident,
 489 however, the accuracy at some western rain gauges outside the 2500 m contour changes little and even
 490 gets worse. This highlights the importance of high-density rain gauge data for precipitation merging, as
 491 demonstrated in many previous works that rain gauge density greatly impacts the accuracy of the
 492 produced dataset (Berndt et al., 2014; Giron et al., 2015; Xie et al., 2007). Therefore, the TPHiPr may
 493 still have large uncertainties in the west of the TP and regions where rain gauges are sparse.



494

495 **Figure 15:** Comparison of the probability density function by (a) precipitation frequency and (b) amount
 496 for rain gauge data and the four datasets. The x axis is in log space.

497 Besides, previous studies have reported that atmospheric simulation-based datasets generally
 498 overestimate the precipitation frequency (Hu and Yuan, 2021; P. Li et al., 2020). Therefore, we
 499 investigate the probability distribution function (PDF) of both precipitation frequency and amount in
 500 TPHiPr with respect to different precipitation intensities. As shown in Fig. 15, the TPHiPr largely
 501 overestimates the frequency of light precipitation (less than 5 mm day⁻¹), although the overestimation is
 502 smaller than that in ERA5L, MSWEP V2 and AERA5. In addition, we can find from Fig. 15b that the
 503 TPHiPr overestimates the amount of light to moderate precipitation but underestimates the amount of
 504 heavy precipitation, and the same is also found in ERA5L, MSWEP V2 and AERA5. Particularly, Fig.
 505 15 shows that the satellite-based IMERG has relatively good performance in reproducing the PDF of
 506 precipitation frequency and amount, indicating that the IMERG can be an effective data source for
 507 correcting the PDF of precipitation. Besides, some previous works have reported that considering both
 508 occurrence and amount of precipitation could contribute to better precipitation merging results compared
 509 to only correcting the precipitation amount (Zhang et al., 2021; Zhu et al, 2022), therefore, methods
 510 including both precipitation occurrence and amount correction should be considered in precipitation
 511 merging in the future.

512 **6. Conclusion**

513 This study collects more than 9000 rain gauges over and around the Third Pole (TP) region from multiple
514 sources. Then, the following steps are applied for merging the high-density gauge observations and the
515 atmospheric simulation-based ERA5_CNN: first, the monthly precipitation climatology at gauge
516 locations is obtained by correcting the climatology of ERA5_CNN with rain gauge data and the monthly
517 climatology at gauge locations is interpolated using a RF and Kriging based method; second, the ratios
518 of observed monthly/daily precipitation to the climatology at gauge locations are interpolated for each
519 month/day using the RF-based method; third, the monthly/daily precipitation fields are obtained by
520 multiplying the interpolated monthly climatology by the interpolated monthly/daily ratios and then
521 adding the residual fields; finally, the daily precipitation fields are further adjusted using the monthly
522 precipitation. Eventually, a long-term (1979-2020) high-resolution ($1/30^\circ$, daily) precipitation dataset
523 (TPHiPr) is produced for the TP.

524 We compare the performance of the merged TPHiPr with the original ERA5_CNN data and four widely-
525 used precipitation datasets, including ERA5L, IMERG, MSWEP V2 and AERA5. Results show that the
526 TPHiPr retains the general spatial patterns of precipitation from ERA5_CNN but has a reduced wet bias
527 in the TP, resulting in better error metrics than ERA5_CNN at most validation gauges. Meanwhile, the
528 TPHiPr generally performs better than the four widely-used precipitation datasets in the TP, with respect
529 to errors in both precipitation amount and detection skill. Validation with 197 independent gauges shows
530 that the TPHiPr has a small relative bias (0.9%), low RMSE (5.0 mm day⁻¹), high correlation (0.76) and
531 high detection skill (CSI=0.61). In addition, the TPHiPr is skillful in detecting extreme precipitation
532 events, although it overestimates the frequency but underestimates the intensity of extreme precipitation.

533 In summary, a new high-accuracy precipitation dataset is produced for the data-sparse TP, which can be
534 used for land surface modeling, water resource management, water-related disaster assessment, climate
535 change research, et al. This dataset is expected to deepen our understanding of land surface processes
536 and water cycles in the TP. Nevertheless, further efforts (e.g. setting up more rain gauges in remote
537 regions and developing more skillful merging methods) are still needed for obtaining higher-accuracy
538 precipitation datasets for the TP, as clarified in section 5, the produced data may still have large
539 uncertainties in data-sparse regions and cannot reproduce the observed frequency and intensity of
540 precipitation well.

541 **Data and code availability**

542 The TPhIPr precipitation dataset in NETCDF format is available at the National Tibetan Plateau Data
543 Center, which can be accessed by <https://doi.org/10.11888/Atmos.tpd.c.272763> (Yang and Jiang, 2022).

544 The codes used for producing this dataset are available upon request to the authors.

545 **Author contributions:** **Yaozhi Jiang:** Conceptualization, Investigation, Formal analysis, Methodology,
546 Software, Visualization, Writing – original draft preparation; **Kun Yang:** Conceptualization, Data
547 curation, Funding acquisition, Project administration, Resources, Supervision, Writing – review &
548 editing; **Youcun Qi:** Data curation, Validation, Writing – review & editing; **Xu Zhou** and **Jie He:**
549 Methodology, Writing – review & editing; **Hui Lu** and **Xin Li:** Supervision, Writing – review & editing;
550 **Yingying Chen:** Data curation, Writing – review & editing; **Xiaodong Li:** Data curation; **Bingrong**
551 **Zhou, Ali Mamtimin, Changkun Shao, Xiaogang Ma, Jiaxin Tian, and Jianhong Zhou:** Writing –
552 review & editing.

553 **Acknowledgements:** This work is supported by the Second Tibetan Plateau Scientific Expedition and
554 Research Program (STEP) (Grant No. 2019QZKK0206), Basic Science Center for Tibetan Plateau Earth
555 System of National Science Foundation of China (Grant No. 41988101), and the National Key Research
556 and Development Program of China (Grant No. 2018YFC1507505).

557 **Competing interests:** The authors declare that they have no conflict of interest.

558

559 **References**

- 560 Alazzy, A.A., Lü H., Chen, R., Ali, A.B., Zhu, Y., Su, J.: Evaluation of Satellite Precipitation Products
561 and Their Potential Influence on Hydrological Modeling over the Ganzi River Basin of the Tibetan
562 Plateau, *Adv. Meteorol.*, 2017, 1-23, <https://doi.org/10.1155/2017/3695285>, 2017.
- 563 Araki, S., Yamamoto, K., Kondo, A.: Application of regression kriging to air pollutant concentrations in
564 Japan with high spatial resolution, *Aerosol Air Qual. Res.*, 15, 234–241.
565 <https://doi.org/10.4209/aaqr.2014.01.0011>, 2015
- 566 Baez-Villanueva, O.M., Zambrano-Bigiarini, M., Beck, H.E., McNamara, I., Ribbe, L., Nauditt, A.,
567 Birkel, C., Verbist, K., Giraldo-Osorio, J.D., Xuan Thinh, N.: RF-MEP: A novel Random Forest
568 method for merging gridded precipitation products and ground-based measurements, *Remote Sens.*
569 *Environ.*, 239, 111606, <https://doi.org/10.1016/j.rse.2019.111606>, 2020.
- 570 Beck, H.E., Wood, E.F., Pan, M., Fisher, C.K., Miralles, D.G., Van Dijk, A.I.J.M., McVicar, T.R., Adler,
571 R.F.: MSWEP v2 Global 3-hourly 0.1 ° precipitation: Methodology and quantitative assessment,
572 *Bull. Am. Meteorol. Soc.*, 100, 473–500, <https://doi.org/10.1175/BAMS-D-17-0138.1>, 2019.
- 573 Berndt, C., Rabiei, E., Haberlandt, U.: Geostatistical merging of rain gauge and radar data for high
574 temporal resolutions and various station density scenarios, *J. Hydrol.*, 508, 88–101,
575 <https://doi.org/10.1016/j.jhydrol.2013.10.028>, 2014.
- 576 Breiman, L.: Random Forests, *Mach. Learn.*, 45, 5–32, https://doi.org/10.1007/978-3-030-62008-0_35,
577 2001.
- 578 Cellura, M., Cirrincione, G., Marvuglia, A., Miraoui, A.: Wind speed spatial estimation for energy
579 planning in Sicily: A neural kriging application, *Renew. Energy*, 33, 1251–1266.
580 <https://doi.org/10.1016/j.renene.2007.08.013>, 2008.
- 581 Chen, F., Ding, L., Piao, S., Zhou, T., Xu, B., Yao, T., Li, X.: The Tibetan Plateau as the engine for Asian
582 environmental change: the Tibetan Plateau Earth system research into a new era, *Sci. Bull.*, 66,
583 1263–1266, <https://doi.org/10.1016/j.scib.2021.04.017>, 2021.
- 584 Chen, R., Song, Y., Kang, E., Han, C., Liu, J., Yang, Y., Qing, W., Liu, Z.: A cryosphere-hydrology
585 observation system in a small alpine watershed in the Qilian mountains of China and its
586 meteorological gradient, *Arctic, Antarct. Alp. Res.*, 46, 505–523, <https://doi.org/10.1657/1938-4246-46.2.505>, 2014.
- 587

588 Chen, R., Song, Y., Liu, J., Yang, Y., Qing, W., Liu, Z., Han, C.: Evaporation and precipitation dataset
589 in Hulugou outlet in Upstream of Heihe River (2011), Natl. Tibet. Plateau Data Cent. [data set],
590 <https://dx.doi.org/10.3972/heihe.110.2013.db>, 2015.

591 Contractor, S., Donat, M.G., Alexander, L. V., Ziese, M., Meyer-Christoffer, A., Schneider, U.,
592 Rustemeier, E., Becker, A., Durre, I., Vose, R.S.: Rainfall Estimates on a Gridded Network
593 (REGEN) - A global land-based gridded dataset of daily precipitation from 1950 to 2016, *Hydrol.*
594 *Earth Syst. Sci.*, 24, 919–943, <https://doi.org/10.5194/hess-24-919-2020>, 2020.

595 Cui, P., Jia, Y.: Mountain hazards in the Tibetan Plateau: Research status and prospects, *Natl. Sci. Rev.*,
596 2, 397–399, <https://doi.org/10.1093/nsr/nwv061>, 2015.

597 Curio, J., Maussion, F., Scherer, D.: A 12-year high-resolution climatology of atmospheric water
598 transport over the Tibetan Plateau, *Earth Syst. Dyn.*, 6, 109–124, [https://doi.org/10.5194/esd-6-](https://doi.org/10.5194/esd-6-109-2015)
599 109-2015, 2015.

600 Demyanov, V., Kanevsky, M., Chernov, S., Savelieva, E., Timonin, V.: Neural Network Residual
601 Kriging Application for Climatic Data, *J. Geogr. Inf. Decis. Anal.*, 2, 215–232, 1998.

602 Gao, H., Wang, J., Yang, Y., Pan, X., Ding, Y., Duan, Z.: Permafrost Hydrology of the Qinghai-Tibet
603 Plateau: A Review of Processes and Modeling, *Front. Earth Sci.*, 8, 1–13,
604 <https://doi.org/10.3389/feart.2020.576838>, 2021.

605 Gao, Y., Chen, F., Jiang, Y.: Evaluation of a convection-permitting modeling of precipitation over the
606 Tibetan Plateau and its influences on the simulation of snow-cover fraction, *J. Hydrometeorol.*, 21,
607 1531–1548, <https://doi.org/10.1175/JHM-D-19-0277.1>, 2020.

608 Gao, Y., Xu, J., Chen, D.: Evaluation of WRF mesoscale climate simulations over the Tibetan Plateau
609 during 1979-2011, *J. Clim.*, 28, 2823–2841, <https://doi.org/10.1175/JCLI-D-14-00300.1>, 2015.

610 Giron, L.M., Wennerström, H., Nordén, L.Å., Seibert, J.: Location and density of rain gauges for the
611 estimation of spatial varying precipitation, *Geogr. Ann. Ser. A Phys. Geogr.*, 97, 167–179,
612 <https://doi.org/10.1111/geoa.12094>, 2015.

613 Hamada, A., Arakawa, O., Yatagai, A.: An automated quality control method for daily rain-gauge data,
614 *Glob. Environ. Res.*, 15, 183–192, 2011.

615 He, J., Yang, K., Tang, W., Lu, H., Qin, J., Chen, Y., Li, X.: The first high-resolution meteorological
616 forcing dataset for land process studies over China, *Sci. Data*, 7, 1–11,

617 <https://doi.org/10.1038/s41597-020-0369-y>, 2020.

618 He, X., Chaney, N.W., Schleiss, M., Sheffield, J.: Spatial downscaling of precipitation using adaptable
619 random forests, *Water Resour. Res.*, 52, 8217–8237, [https://doi.org/10.1111/j.1752-](https://doi.org/10.1111/j.1752-1688.1969.tb04897.x)
620 1688.1969.tb04897.x, 2016.

621 Hersbach, H., Bell, B., Berrisford, P., Hirahara, S., Horányi, A., Muñoz-Sabater, J., Nicolas, J., Peubey,
622 C., Radu, R., Schepers, D., Simmons, A., Soci, C., Abdalla, S., Abellan, X., Balsamo, G., Bechtold,
623 P., Biavati, G., Bidlot, J., Bonavita, M., De Chiara, G., Dahlgren, P., Dee, D., Diamantakis, M.,
624 Dragani, R., Flemming, J., Forbes, R., Fuentes, M., Geer, A., Haimberger, L., Healy, S., Hogan,
625 R.J., Hólm, E., Janisková, M., Keeley, S., Laloyaux, P., Lopez, P., Lupu, C., Radnoti, G., de
626 Rosnay, P., Rozum, I., Vamborg, F., Villaume, S., Thépaut, J.N.: The ERA5 global reanalysis, *Q. J. R. Meteorol. Soc.*, 146, 1999–2049, <https://doi.org/10.1002/qj.3803>, 2020.

628 Hong, Z., Han, Z., Li, X., Long, D., Tang, G., Wang, J.: Generation of an improved precipitation dataset
629 from multisource information over the tibetan plateau, *J. Hydrometeorol.*, 22, 1275–1295,
630 <https://doi.org/10.1175/JHM-D-20-0252.1>, 2021.

631 Hu, X., Yuan, W.: Evaluation of ERA5 precipitation over the eastern periphery of the Tibetan plateau
632 from the perspective of regional rainfall events, *Int. J. Climatol.*, 41, 2625–2637,
633 <https://doi.org/10.1002/joc.6980>, 2021.

634 Huai, B., Wang, J., Sun, W., Wang, Y., Zhang, W.: Evaluation of the near-surface climate of the recent
635 global atmospheric reanalysis for Qilian Mountains, Qinghai-Tibet Plateau, *Atmos. Res.*, 250,
636 105401, <https://doi.org/10.1016/j.atmosres.2020.105401>, 2021.

637 Huffman, G.J., Adler, R.F., Bolvin, D.T., Gu, G., Nelkin, E.J., Bowman, K.P., Hong, Y., Stocker, E.F.,
638 Wolff, D.B.: The TRMM Multisatellite Precipitation Analysis (TMPA): Quasi-global, multiyear,
639 combined-sensor precipitation estimates at fine scales, *J. Hydrometeorol.*, 8, 38–55,
640 <https://doi.org/10.1175/JHM560.1>, 2007.

641 Huffman, G.J., Bolvin, D.T., Braithwaite, D., Hsu, K., Kidd, R.J.C., Nelkin, E.J., Sorooshian, S., Tan, J.,
642 Xie, P.: Algorithm Theoretical Basis Document (ATBD) NASA Global Precipitation
643 Measurement (GPM) Integrated Multi-satellite Retrievals for GPM (IMERG), NASA 29, 2019.

644 Immerzeel, W.W., Wanders, N., Lutz, A.F., Shea, J.M., Bierkens, M.F.P.: Reconciling high-altitude
645 precipitation in the upper Indus basin with glacier mass balances and runoff, *Hydrol. Earth Syst.*

646 Sci., 19, 4673–4687, <https://doi.org/10.5194/hess-19-4673-2015>, 2015.

647 Jiang, Y., Yang, K., Li, Xiaodong, Zhang, W., Shen, Y., Chen, Y., Li, Xin: Atmospheric simulation-
648 based precipitation datasets outperform satellite-based products in closing basin-wide water budget
649 in the eastern Tibetan Plateau, *Int. J. Climatol.*, 1–17, <https://doi.org/10.1002/joc.7642>, 2022.

650 Jiang, Y., Yang, K., Shao, C., Zhou, X., Zhao, L., Chen, Y.: A downscaling approach for constructing
651 high-resolution precipitation dataset over the Tibetan Plateau from ERA5 reanalysis, *Atmos. Res.*,
652 256, 105574, <https://doi.org/10.1016/j.atmosres.2021.105574>, 2021.

653 Jiang, Y., Yang, K., Yang, H., Lu, H., Chen, Y., Zhou, X., Sun, J., Yang, Y., Wang, Y.: Characterizing
654 basin-scale precipitation gradients in the Third Pole region using a high-resolution atmospheric
655 simulation-based dataset, *Hydrol. Earth Syst. Sci.*, 26, 4587–4601, <https://doi.org/10.5194/hess-26-4587-2022>, 2022.

656

657 Katsanos, D., Retalis, A., Tymvios, F., Michaelides, S.: Analysis of precipitation extremes based on
658 satellite (CHIRPS) and in situ dataset over Cyprus, *Nat. Hazards*, 83, 53–63,
659 <https://doi.org/10.1007/s11069-016-2335-8>, 2016.

660 Li, D., Yang, K., Tang, W., Li, X., Zhou, X., Guo, D.: Characterizing precipitation in high altitudes of
661 the western Tibetan plateau with a focus on major glacier areas, *Int. J. Climatol.*, 1–14,
662 <https://doi.org/10.1002/joc.6509>, 2020.

663 Li, K., Tian, F., Khan, M.Y.A., Xu, R., He, Z., Yang, L., Lu, H., Ma, Y.: A high-accuracy rainfall dataset
664 by merging multiple satellites and dense gauges over the southern Tibetan Plateau for 2014–2019
665 warm seasons, *Earth Syst. Sci. Data*, 13, 5455–5467, <https://doi.org/10.5194/essd-13-5455-2021>,
666 2021.

667 Li, P., Furtado, K., Zhou, T., Chen, H., Li, J.: Convection-permitting modelling improves simulated
668 precipitation over the central and eastern Tibetan Plateau, *Q. J. R. Meteorol. Soc.*, 1–22,
669 <https://doi.org/10.1002/qj.3921>, 2020.

670 Li, Y., Pang, B., Ren, M., Shi, S., Peng, D., Zhu, Z., Zuo, D.: Evaluation of Performance of Three
671 Satellite-Derived Precipitation Products in Capturing Extreme Precipitation Events over Beijing,
672 China, *Remote Sens*, 14, 2698, <https://doi.org/10.3390/rs14112698>, 2022.

673 Lockhoff, M., Zolina, O., Simmer, C., Schulz, J.: Evaluation of satellite-retrieved extreme precipitation
674 over Europe using gauge observations, *J. Clim.*, 27, 607–623, [32](https://doi.org/10.1175/JCLI-D-13-</p></div><div data-bbox=)

675 00194.1, 2014.

676 Lu, D., Yong, B.: Evaluation and hydrological utility of the latest GPM IMERG V5 and GSMaP V7
677 precipitation products over the Tibetan Plateau, *Remote Sens.*, 10,
678 <https://doi.org/10.3390/rs10122022>, 2018.

679 Lundquist, J., Hughes, M., Gutmann, E., Kapnick, S.: Our skill in modeling mountain rain and snow is
680 bypassing the skill of our observational networks, *Bull. Am. Meteorol. Soc.*, 2473–2490,
681 <https://doi.org/10.1175/BAMS-D-19-0001.1>, 2019.

682 Luo, L.: Meteorological observation data from the integrated observation and research station of the
683 alpine environment in Southeast Tibet (2007-2017), Natl. Tibet. Plateau Data Cent.[data set],
684 <https://doi.org/10.11888/AtmosphericPhysics.tpe.68.db>, 2018.

685 Ma, Y., Hong, Y., Chen, Y., Yang, Y., Tang, G., Yao, Y., Long, D., Li, C., Han, Z., Liu, R.: Performance
686 of Optimally Merged Multisatellite Precipitation Products Using the Dynamic Bayesian Model
687 Averaging Scheme Over the Tibetan Plateau, *J. Geophys. Res. Atmos.*, 123, 814–834,
688 <https://doi.org/10.1002/2017JD026648>, 2018.

689 Ma, Y., Zhang, Y., Yang, D., Farhan, S. B.: Precipitation bias variability versus various gauges under
690 different climatic conditions over the Third Pole Environment (TPE) region, *Int. J. Climatol.*, 35,
691 1201–1211, <https://doi.org/10.1002/joc.4045>, 2015.

692 Ma, Z., Xu, J., Zhu, S., Yang, J., Tang, G., Yang, Y., Shi, Z., Hong, Y.: AIMERG: A new Asian
693 precipitation dataset (0.1 °half-hourly, 2000-2015) by calibrating the GPM-era IMERG at a daily
694 scale using APHRODITE, *Earth Syst. Sci. Data*, 12, 1525–1544, [https://doi.org/10.5194/essd-12-](https://doi.org/10.5194/essd-12-1525-2020)
695 1525-2020, 2020.

696 Ma, Z., Xu, J., Ma, Y., Zhu, S., He, K., Zhang, S., Ma, W., Xu, X.: A Long-Term Asian Precipitation
697 Dataset (0.1 °, 1-hourly, 1951–2015, Asia) Anchoring the ERA5-Land under the Total Volume
698 Control by APHRODITE, *Bull. Am. Meteorol. Soc.*, 1146–1171, [https://doi.org/10.1175/BAMS-](https://doi.org/10.1175/BAMS-D-20-0328.1)
699 D-20-0328.1, 2022.

700 Maussion, F., Scherer, D., Mäg, T., Collier, E., Curio, J., Finkelnburg, R.: Precipitation seasonality and
701 variability over the Tibetan Plateau as resolved by the high Asia reanalysis, *J. Clim.*, 27, 1910–
702 1927, <https://doi.org/10.1175/JCLI-D-13-00282.1>, 2014.

703 Menne, M.J., Durre, I., Vose, R.S., Gleason, B.E., Houston, T.G.: An overview of the global historical

704 climatology network-daily database, *J. Atmos. Ocean. Technol.*, 29, 897–910,
705 <https://doi.org/10.1175/JTECH-D-11-00103.1>, 2012.

706 Muñoz-Sabater, J., Dutra, E., Agustín-Panareda, A., Albergel, C., Arduini, G., Balsamo, G., Boussetta, S.,
707 Choulga, M., Harrigan, S., Hersbach, H., Martens, B., Miralles, D.G., Piles, M., Rodríguez-
708 Fernández, N.J., Zsoter, E., Buontempo, C., Thépaut, J.N.: ERA5-Land: A state-of-the-art global
709 reanalysis dataset for land applications, *Earth Syst. Sci. Data*, 13, 4349–4383,
710 <https://doi.org/10.5194/essd-13-4349-2021>, 2021.

711 Norris, J., Carvalho, L.M.V., Jones, C., Cannon, F., Bookhagen, B., Palazzi, E., Tahir, A.A.: The
712 spatiotemporal variability of precipitation over the Himalaya: evaluation of one-year WRF model
713 simulation, *Clim. Dyn.*, 49, 2179–2204, <https://doi.org/10.1007/s00382-016-3414-y>, 2017.

714 Ouyang, L., Lu, H., Yang, K., Leung, L.R., Wang, Y., Zhao, L., Zhou, X., LaZhu, Chen, Y., Jiang, Y.,
715 Yao, X.: Characterizing uncertainties in ground “truth” of precipitation over complex terrain
716 through high-resolution numerical modeling, *Geophys. Res. Lett.*, 1–11,
717 <https://doi.org/10.1029/2020gl091950>, 2021.

718 Savéan, M., Delclaux, F., Chevallier, P., Wagnon, P., Gonga-Saholiariliva, N., Sharma, R., Neppel, L.,
719 Arnaud, Y.: Water budget on the Dudh Koshi River (Nepal): Uncertainties on precipitation, *J.*
720 *Hydrol.*, 531, 850–862, <https://doi.org/10.1016/j.jhydrol.2015.10.040>, 2015.

721 Schamm, K., Ziese, M., Becker, A., Finger, P., Meyer-Christoffer, A., Schneider, U., Schröder, M.,
722 Stender, P.: Global gridded precipitation over land: A description of the new GPCC First Guess
723 Daily product, *Earth Syst. Sci. Data*, 6, 49–60, <https://doi.org/10.5194/essd-6-49-2014>, 2014.

724 Sekulić, A., Kilibarda, M., Protić, D., Bajat, B.: A high-resolution daily gridded meteorological dataset
725 for Serbia made by Random Forest Spatial Interpolation, *Sci. Data*, 8, 1–12,
726 <https://doi.org/10.1038/s41597-021-00901-2>, 2021.

727 Shen, Y., Xiong, A., Hong, Y., Yu, J., Pan, Y., Chen, Z., Saharia, M.: Uncertainty analysis of five
728 satellite-based precipitation products and evaluation of three optimally merged multi-algorithm
729 products over the Tibetan Plateau, *Int. J. Remote Sens.*, 35, 6843–6858,
730 <https://doi.org/10.1080/01431161.2014.960612>, 2014.

731 Sugimoto, S., Ueno, K., Fujinami, H., Nasuno, T., Sato, T., Takahashi, H.G.: Cloud-Resolving-Model
732 Simulations of Nocturnal Precipitation over the Himalayan Slopes and Foothills, *J. Hydrometeorol.*,

733 22, 3171–3188, <https://doi.org/10.1175/JHM-D-21-0103.1>, 2021.

734 Tan, X., Ma, Z., He, K., Han, X., Ji, Q., He, Y.: Evaluations on gridded precipitation products spanning
735 more than half a century over the Tibetan Plateau and its surroundings, *J. Hydrol.*, 582,
736 <https://doi.org/10.1016/j.jhydrol.2019.124455>, 2020.

737 Wang, A., Zeng, X.: Evaluation of multireanalysis products with in situ observations over the Tibetan
738 Plateau, *J. Geophys. Res. Atmos.*, 117, 1–12, <https://doi.org/10.1029/2011JD016553>, 2012.

739 Wang, J.: Daily meteorological Data of Nam Co Station China during 2019-2020, *Natl. Tibet. Plateau*
740 *Data Cent.*[data set], <https://doi.org/10.11888/Meteoro.tpsc.271782>, 2021.

741 Wang, X., Pang, G., Yang, M.: Precipitation over the tibetan plateau during recent decades: A review
742 based on observations and simulations, *Int. J. Climatol.*, 38, 1116–1131,
743 <https://doi.org/10.1002/joc.5246>, 2018.

744 Wang, X., Tolksdorf, V., Otto, M., Scherer, D.: WRF-based dynamical downscaling of ERA5 reanalysis
745 data for High Mountain Asia: Towards a new version of the High Asia Refined analysis, *Int. J.*
746 *Climatol.*, 1–20, <https://doi.org/10.1002/joc.6686>, 2020.

747 Wang, Y., Wang, L., Li, X., Zhou, J., Hu, Z.: An integration of gauge, satellite, and reanalysis
748 precipitation datasets for the largest river basin of the Tibetan Plateau, *Earth Syst. Sci. Data*, 12,
749 1789–1803, <https://doi.org/10.5194/essd-12-1789-2020>, 2020a.

750 Wang, Y., Yang, K., Zhou, X., Chen, D., Lu, H., Ouyang, L., Chen, Y., Lazhu, Wang, B.: Synergy of
751 orographic drag parameterization and high resolution greatly reduces biases of WRF-simulated
752 precipitation in central Himalaya, *Clim. Dyn.*, 54, 1729–1740, [https://doi.org/10.1007/s00382-](https://doi.org/10.1007/s00382-019-05080-w)
753 [019-05080-w](https://doi.org/10.1007/s00382-019-05080-w), 2020b.

754 Wang, Y., Yang, K., Zhou, X., Wang, B., Chen, D., Lu, H., Lin, C., Zhang, F.: The Formation of a Dry-
755 Belt in the North Side of Central Himalaya Mountains, *Geophys. Res. Lett.*, 46, 2993–3000,
756 <https://doi.org/10.1029/2018GL081061>, 2019.

757 Wei, D., Wang, X.: Meteorological observation data in an alpine steppe site of Shenzha Station (2015-
758 018), *Natl. Tibet. Plateau Data Cent.*[data set], <https://doi.org/10.11888/Meteoro.tpsc.270117>,
759 2019.

760 Willmott, C.J., Robeson, S.M.: Climatologically aided interpolation (CAI) of terrestrial air temperature,
761 *Int. J. Climatol.*, 15, 221–229, <https://doi.org/10.1002/joc.3370150207>, 1995.

762 Xie, P., Yatagai, A., Chen, M., Hayasaka, T., Fukushima, Y., Liu, C., Yang, S.: A gauge-based analysis
763 of daily precipitation over East Asia, *J. Hydrometeorol.*, 8, 607–626,
764 <https://doi.org/10.1175/JHM583.1>, 2007.

765 Xu, J., Ma, Z., Yan, S., Peng, J.: Do ERA5 and ERA5-land precipitation estimates outperform satellite-
766 based precipitation products? A comprehensive comparison between state-of-the-art model-based
767 and satellite-based precipitation products over mainland China, *J. Hydrol.*, 605, 127353,
768 <https://doi.org/10.1016/j.jhydrol.2021.127353>, 2022.

769 Xu, R., Tian, F., Yang, L., Hu, H., Lu, H., Hou, A.: Ground validation of GPM IMERG and trmm
770 3B42V7 rainfall products over Southern Tibetan plateau based on a high-density rain gauge
771 network, *J. Geophys. Res.*, 122, 910–924, <https://doi.org/10.1002/2016JD025418>, 2017.

772 Yang, K., Jiang, Y.: A long-term (1979–2020) high-resolution (1/30 °) precipitation dataset for the Third
773 Polar region (TPHiPr), *Natl. Tibet. Plateau Data Cent.* [data set],
774 <https://doi.org/10.11888/Atmos.tpdc.272763>, 2022.

775 Yang, S., Li, R., Wu, T., Hu, G., Xiao, Y., Du, Y., Zhu, X., Ni, J., Ma, J., Zhang, Y., Shi, J., Qiao, Y.:
776 Evaluation of reanalysis soil temperature and soil moisture products in permafrost regions on the
777 Qinghai-Tibetan Plateau, *Geoderma*, 377, 114583,
778 <https://doi.org/10.1016/j.geoderma.2020.114583>, 2020.

779 Yang, W., Yao, T., Zhu, M., Wang, Y.: Comparison of the meteorology and surface energy fluxes of
780 debris-free and debris-covered glaciers in the southeastern Tibetan Plateau, *J. Glaciol.*, 63, 1090–
781 1104, <https://doi.org/10.1017/jog.2017.77>, 2017.

782 Yang, W.: Conventional ice surface meteorological data for Parlung Glacier No. 4 and Debris-covered
783 24K Glacier in southeast Tibet from June to September (2016), *Natl. Tibet. Plateau Data Cent.*[data
784 set], <https://doi.org/10.11888/AtmosPhys.tpe.249475.db>, 2018.

785 Yao, T., Bolch, T., Chen, D., Gao, J., Immerzeel, W., Piao, S., Su, F., Thompson, L., Wada, Y., Wang,
786 L., Wang, T., Wu, G., Xu, B., Yang, W., Zhang, G., Zhao, P.: The imbalance of the Asian water
787 tower, *Nat. Rev. Earth Environ.*, <https://doi.org/10.1038/s43017-022-00299-4>, 2022.

788 Yatagai, A., Kamiguchi, K., Arakawa, O., Hamada, A., Yasutomi, N., Kitoh, A.: Aphrodite constructing
789 a long-term daily gridded precipitation dataset for Asia based on a dense network of rain gauges,
790 *Bull. Am. Meteorol. Soc.*, 93, 1401–1415, <https://doi.org/10.1175/BAMS-D-11-00122.1>, 2012.

791 Ye, B., Yang, D., Ding, Y., Han, T., Koike, T.: A bias-corrected precipitation climatology for China, *J.*
792 *Hydrometeorol.*, 62, 3–13 , <https://doi.org/10.1175/JHM-366.1>, 2007.

793 You, Q., Fraedrich, K., Ren, G., Ye, B., Meng, X., Kang, S.: Inconsistencies of precipitation in the eastern
794 and central Tibetan Plateau between surface adjusted data and reanalysis, *Theor. Appl. Climatol.*,
795 109, 485–496, <https://doi.org/10.1007/s00704-012-0594-1>, 2012.

796 Zhang, G.: Dataset of river basins map over the TP (2016), *Natl. Tibet. Plateau Data Cent.*[data set],
797 <https://doi.org/10.11888/BaseGeography.tpe.249465.file>, 2019.

798 Zhang, L., Li, X., Zheng, D., Zhang, K., Ma, Q., Zhao, Y., Ge, Y.: Merging multiple satellite-based
799 precipitation products and gauge observations using a novel double machine learning approach, *J.*
800 *Hydrol.*, 594, 125969, <https://doi.org/10.1016/j.jhydrol.2021.125969>, 2021.

801 Zhang, Y.: Meteorological observation dataset of Shiquan River Source (2012-2015), *Natl. Tibet. Plateau*
802 *Data Cent.*[data set], <https://doi.org/10.11888/Meteoro.tpsc.270548>, 2018.

803 Zhao, L., Wu, T., Xie, C., Li, R., Wu, X., Yao, J., Yue, G., Xiao, Y.: Support Geoscience Research,
804 Environmental Management, and Engineering Construction with Investigation and Monitoring on
805 Permafrost in the Qinghai-Tibet Plateau, China. *Bull. Chinese Acad. Sci. (Chinese Version)*, 32,
806 1159–1168, <https://doi.org/10.16418/j.issn.1000-3045.2017.10.015>, 2017.

807 Zhao, L.: Meteorological Datasets of Xidatan station (XDT) on the Tibetan Plateau in 2014-2018, *Natl.*
808 *Tibet. Plateau Data Cent.*[data set], <https://doi.org/10.11888/Meteoro.tpsc.270084>, 2018.

809 Zhou, X., Yang, K., Ouyang, L., Wang, Y., Jiang, Y., Li, X., Chen, D., Prein, A.: Added value of
810 kilometer-scale modeling over the third pole region: a CORDEX-CPTP pilot study, *Clim. Dyn.*,
811 <https://doi.org/10.1007/s00382-021-05653-8>, 2021.

812 Zhu, S., Ma, Z., Xu, J., He, K., Liu, H., Ji, Q., Tang, G., Hu, H., Gao, H.: A Morphology-Based
813 Adaptively Spatio-Temporal Merging Algorithm for Optimally Combining Multisource Gridded
814 Precipitation Products with Various Resolutions, *IEEE Trans. Geosci. Remote Sens.*, 60,
815 <https://doi.org/10.1109/TGRS.2021.3097336>, 2022.

816